scientific reports

Check for updates

OPEN

Mineralization and metallogenic model of the Laurani high-sulfidation epithermal deposit in northeastern Bolivian Altiplano

Fei Liu[1,3], Runsheng Han[2,3]✉, Shuming Wen[2], Dong Zhao[2,3]✉, Wenyao Li[2,3], Li Lei[2], Chaojian Qin[4] & Yuxinyue Guo[1]

The Laurani high-sulfidation epithermal deposit, located in the northeastern Altiplano of Bolivia, is a representative gold-polymetallic deposit linked to the late Miocene volcanic rocks that were formed approximately at about 7.5 Ma. At Laurani, four mineralization stages are defined. Stage I primarily consists of ore-barren vuggy quartz that free with metal sulfides. Stage II and stage III generate four predominant styles of mineralization of explosive breccia-style Au–Cu, contact-style Cu–Au–Ag, hydrothermal vein-style Au–Ag–Cu–Pb–Zn and porphyry-style Au–Cu that with a diversity of occurrences, reflecting the strong lithological and structural controls. Stage IV is formed by supergene oxidation of earlier metalliferous minerals postdated the main mineralization. Hydrothermal alteration is characterized by significant intensity and zoning, with phyllic alteration at the center, surrounded by propylitic alteration, and further overlapped by extensive argillic alteration. Additionally, the well-developed quartz–alunite–barite tends to be found along or in close proximity to the hydrothermal vein-style orebodies. Fluid inclusions hosted in the stage I ore-barren quartz indicate that the ore-forming fluids predating predominant metal deposition are low- to moderate-salinity (0.2–23.1 wt.% NaCleq), high-temperature (90% of homogenization temperature > 300 ℃) and CO_2-bearing fluids. Subsequently, through processes of boiling (~ 250 to 360 ℃), cooling and mixing with meteoric water, these fluids transform to low-salinity (4.2–6.9 wt.% NaCleq) and low-temperature (90% of homogenization temperature < 220 ℃) fluids. H–O isotopic compositions obtained from the stage I ore-barren quartz and the stage II quartz vein and barite vein have $\delta D = -101.50$ to $-41.31‰$ and $\delta^{18}O_{H2O} = 5.66$ to $12.27‰$, demonstrating a trend extending from magmatic composition to meteoric water, which suggest that the ore-forming fluids are mostly magmatic water, mixing with a little meteoric water. $\delta^{34}S$ values of sulfides from the stage II and stage III are 1.57–5.55‰, while barites from the stage II in textural equilibrium with sulfides own $\delta^{34}S$ values of 24.01–25.90‰, reflecting a magmatic origin and H_2S is the dominant species of sulfur. Pb isotope signatures of Laurani ores ($^{206}Pb/^{204}Pb = 18.2869–18.3568$, $^{207}Pb/^{204}Pb = 15.6082–15.6337$ and $^{208}Pb/^{204}Pb = 38.6937–38.7719$) are consistent with those of the Arequipa Massif basement located beneath the Altiplano, indicating that Pb originates initially from the old, thickened lower crust of the Arequipa Massif. The study on mineralization at Laurani, along with the similar epithermal deposits that formed in the late Miocene in the Central Andes, suggests that the thickened lower crust could play a crucial role as a metal source for forming porphyry–epithermal deposits. Currently, the hydrothermal vein-style Au–Ag–Cu–Pb–Zn is the most important and economic mineralization that developed in the shallow part at Laurani. Moreover, the first discovery of porphyry-style Au–Cu within dacitic porphyry suggests a significant potential for the formation of a porphyry deposit at greater depths in the Laurani mine.

Keywords H–O–S–Pb isotopes, Porphyry–epithermal deposit, Arequipa Massif, Laurani deposit, Altiplano, Central Andes

[1]College of Mining Engineering, Guizhou University of Engineering Science, Bijie 551700, China. [2]Faculty of Land Resources Engineering, Kunming University of Science and Technology, Kunming 650093, China. [3]Southwest Institute of Geological Survey, Geological Survey Center for Non-Ferrous Mineral Resources, Kunming 650093, China. [4]State Key Laboratory of Ore Deposit Geochemistry, Institute of Geochemistry, Chinese Academy of Sciences, Guiyang 550081, China. ✉email: 554670042@qq.com; 494324236@qq.com

Epithermal deposits, proposed initially by Lindgren[1] to describe those formed at low temperatures in the shallow part, are important sources of metals of gold, silver, copper, zinc, lead and selenium, among others. Despite numerous classifications of epithermal deposit have been proposed[2–9], two predominant types of high- and low-sulfidation epithermal deposit are defined attributing to the significant differences of mineral assemblages, hydrothermal alteration features, ore-forming materials and metallogenic environments. The former is related to acid magmatic-hydrothermal systems[6,9], containing the typical high-sulfidation state sulfides and gangue minerals such as tennantite, tetrahedrite, covellite, alunite, kaolinite, and residual vuggy quartz[8], which are rare or absent in the low-sulfidation epithermal deposits. In contrast, the ore-forming fluids in the latter are mainly meteoric water[6], resulting in mineral assemblages with a low-sulfidation state that consist of sphalerite, arsenopyrite, adularia, illite and calcite[6,8]. In many high-sulfidation epithermal deposits, the existence of porphyry deposits had been discovered at depth[10,11], whereas the genetic relationships between porphyry deposits and low-sulfidation epithermal deposits is difficult to demonstrate[11].

The Altiplano is an important polymetallic metallogenic belt within the Central Andes, it primarily contains the sedimentary rock-hosted copper deposits and the epithermal deposits[12–15]. The Laurani deposit is one of the typical high-sulfidation examples that located in the northeastern Altiplano in Bolivia[16], with a long history of exploration and exploitation. At Laurani, a complex gold polymetallic mineralization formed mainly in veins comprised of native gold, pyrite, tennantite, enargite, sphalerite, galena, covellite, etc.[12,16]. Four mineralization styles and significant zonation of metal elements and hydrothermal alteration have been proposed[16,17]. Structural deformation and intermediate-acid magmatism are the dominant ore-controlling factors at Laurani[16,18], and the zircon U–Pb ages demonstrate that the volcanic activity occurred at about 7.5 Ma[19]. Although the Laurani deposit has been of interest for a long time, and the geological features, ore-controlling factors, geochronology and petrogenesis of volcanic rocks has been recently discussed in detail[16,19], the sources of the ore-forming fluids and materials, and the ore-forming processes are still unclear, which restricts the deepened understanding of mineralization at Laurani.

In this paper, new fluid inclusions, H–O, S and Pb isotopes analyses are mainly presented to constrain the characterization and evolution of the ore-forming fluids and the source of the metals. Additionally, the features and processes involved in mineralization are discussed. This contribution may provide a new information of the Laurani high-sulfidation deposit, to understand the ore genesis as well as exploration guides for the similar epithermal deposits in the Central Andes.

Regional geology

The Altiplano, one of six physiographic provinces in Bolivia, located between the Western and Eastern Cordillera (Fig. 1a), which are characterized by a magmatic arc and a fold-and-thrust belt[20], respectively. It is initially an extensive depression and grows with the two-stage uplift of the Central Andes[21–24]. The Altiplano is filled with the Cenozoic continental sediments[25–27], and develops with multiple stages and episodes of structural deformations and magmatic activities[13,25] (Fig. 1b). Numerous epithermal deposits have been formed in the Altiplano and its adjacent regions[15], and they are genetically associated with the middle to late Neogene volcanism and shallow magmatism[13]. These deposits exhibit intense structural control and occur in various mineralization styles[15] (Fig. 1b), and the Laurani deposit is one of the typical representative deposits among them.

Geology of the Laurani deposit

In the Laurani deposit, the strata consist mainly of Miocene conglomerates, sandstones, and siltstones (red beds) and Quaternary sediments (Fig. 2), Silurian and Cretaceous strata distribute in the periphery[16] (Fig. 1b). Ring faults, along with an amount of various trending secondary faults, intrusive contacts and explosive breccia pipes are well developed. The latter three types of structures show an intense control on the shape and spatial distribution of ore (Figs. 2, 3). Four types volcanic rocks of tuff, dacite, dacitic porphyry and monzogranite porphyry that formed contemporaneously at about 7.5 Ma are recognized (Fig. 2), which have a genetic contribution to the gold and polymetallic mineralization[19].

Four styles of mineralization with a diversity of occurrence develop at Laurani, including explosive breccia-style Au–Cu, contact-style Cu–Au–Ag, hydrothermal vein-style Au–Ag–Cu–Pb–Zn, and porphyry-style Au–Cu (Fig. 4). The explosive breccia-style mineralization occurs in stockwork veins (Fig. 4a) and distributes in the explosive breccia pipe (Fig. 3), commonly with a relatively low-grade gold (approximately 0.1–1 g/t) and copper (approximately 0.01–1%). The contact-style mineralization forms mainly in veins, and distributes primarily in the lithologic interface between dacitic porphyry and tuff[16] (Fig. 3). Meanwhile, this type of mineralization can also be observed where volcanic rocks interact with the Miocene red beds[16]. The hydrothermal vein-style mineralization presents in stockwork, vein and veinlet orebodies, and forms usually within tuff, monzogranite porphyry and dacitic porphyry in the shallow part (Fig. 4b–e). Nevertheless, in tuff and monzogranite porphyry, it's characterized by stockwork and veinlet orebodies (Fig. 4b–d), while the large and high-grade orebodies, commonly with massive accumulation of sulfides, tend to occur in dacitic porphyry (Fig. 4e). The hydrothermal vein-style orebodies are the most important and the most economically valuable in the Laurani deposit at present, which comprises mostly of N50°E veins system and N20°E veins system that controlled predominantly by secondary faults (Figs. 2, 3). Dissemination, vein and veinlet orebodies demonstrate in the porphyry-style mineralization that only occurs within dacitic porphyry in the depth (Fig. 4f–g). The metallogenic element assemblages exhibit zoning: vertically, Au–Cu is mainly found at greater depths, whereas Au–Ag–Cu–Pb–Zn is more prevalent at shallower levels; horizontally, Au–Ag–Cu–Pb–Zn and Ag–Pb–Zn are primarily distributed in the northern and southern part, respectively, which are separated by the Huari Humana fault[16].

Hydrothermal alterations are intense and exhibit significant zonation[16,17] (Fig. 3). Horizontal zonation varies from phyllic alteration (pyrite + sericite + quartz) to propylitic alteration (chlorite + epidote ± minor

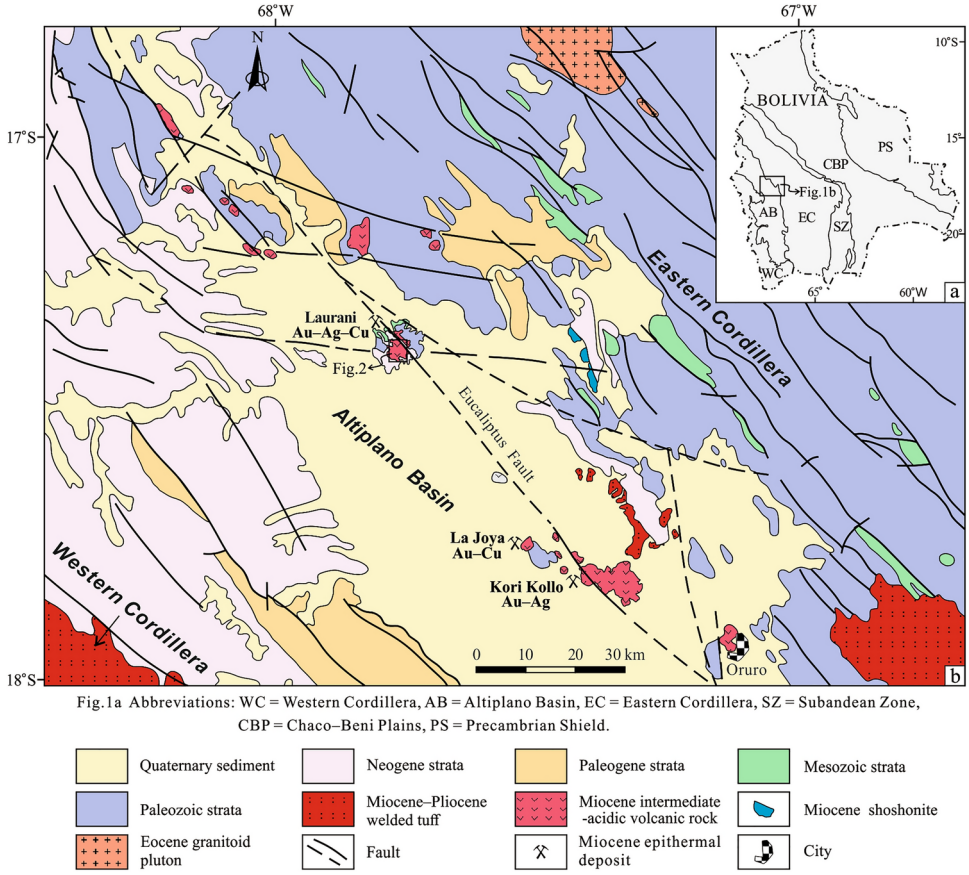

Fig.1a Abbreviations: WC = Western Cordillera, AB = Altiplano Basin, EC = Eastern Cordillera, SZ = Subandean Zone, CBP = Chaco–Beni Plains, PS = Precambrian Shield.

Fig. 1. (**a**) General Location of Fig. 1b (modified after Arce-Burgoa and Goldfarb[15]); (**b**) Geological and structural map with the location of the Laurani deposit and other epithermal and porphyry deposits (modified after Redwood and Rice[18]; SERGEOMIN-YPFB[81]).

carbonate ± minor quartz) and carbonatization (mainly calcite) from the central portion of dacitic porphyries outward. Widespread argillic alteration (kaolinite + dickite + hydromuscovite ± montmorillonite) overlaps on the phyllic and propylitic alteration in the shallow. Quartz–alunitization–baratization (quartz + alunite + barite) is mainly distributed along the hydrothermal vein-style orebodies. Vertically, zonation varies from phyllic to propylitic (not always existed) and argillic alteration, ranging from deeper to shallower areas.

Four mineralization stages are distinguished based on crosscutting relationships, mineral and alteration assemblages (Fig. 5). The stage I consists of ore-barren quartz veins that commonly display a vuggy texture (Fig. 5a).

The stage II tetrahedrite + pyrite + quartz ± barite ± alunite veins represent the main ore-forming stage (Fig. 5b–e). Tetrahedrite is generally coarse-grained crystals in aggregates, a few is disseminated. Pyrite is mainly medium- to coarse-grained, a few is fine-grained in aggregates. Small amount of chalcopyrite and bornite also can be observed in this stage of vein. Quartz is the primary gangue mineral and has always existed with sulfide, but barite and alunite can either form composite veins together or appear as separate, distinct veins. The crosscutting and mineral metasomatic relationships indicate that the tetrahedrite + pyrite + quartz ± barite ± alunite veins postdate the stage I vuggy quartz (Fig. 5a) and precede the latter sphalerite + galena ± calcite ± quartz veins (Fig. 5j).

The stage III sphalerite + galena ± calcite ± quartz veins (Fig. 5g), contain small amounts of pyrite and quartz. With a few of Au and Ag-bearing minerals occur as fine-grains in sphalerite or galena (Fig. 5k–l). Calcite is the main gangue mineral, with occasional occurrences of quartz in micro-fine grains. These veins are mainly distributed in the propylitic zone.

The stage IV chalcanthite ± limonite mineralization is formed through supergene oxidation on the basis of the pre-existing stage II and stage III veins. Keller et al.[28] and Paar et al.[29] have proposed two new minerals, Lammerit and Braithwaiteite, respectively, which are secondary copper minerals discovered at Laurani.

Sampling and analytical methods

Sampling

The 14 analyzed samples were selected for fluid inclusion and isotope study from two drilling holes (ZK2 and ZK4; Fig. 3), four adits (PD2, PD4, PD6 and PD7; Figs. 3 and 6) and the surface of mine. The samples are systematically sorted, described and identified; some pictures of selected samples are shown in Fig. 5. They

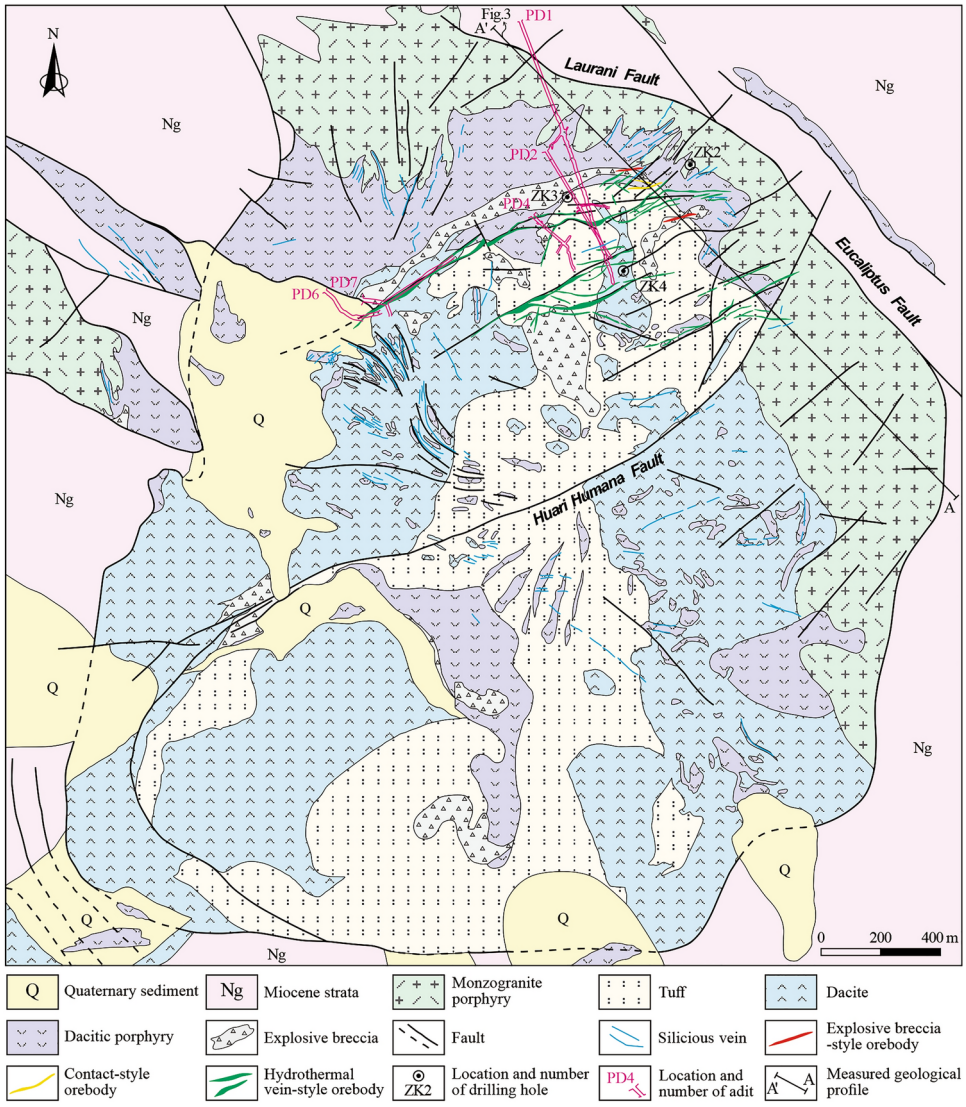

Fig. 2. The geological map of the Laurani deposit (modified after Liu et al.[19]).

are ground into inclusion sheets with a thickness of 0.2 mm. The stage I ore-barren quartz, the stage II quartz eye (described below), quartz vein and barite vein, and the stage III sphalerite are selected for fluid inclusion microthermometry and gas- and solid-phase composition analysis. The stage I ore-barren quartz, the stage II quartz vein and barite vein are selected for H-O isotope analysis. Pyrite, tetrahedrite, sphalerite, galena and barite are utilized for the analysis of sulfur and lead isotopes (excluding barite). Microthermometry and gas- and solid-phase composition analysis are carried out at the Institute of Geochemistry, Chinese Academy of Sciences, Guiyang, P. R. China. All the isotope analysis samples undergo crushing, separating and purifying before measuring, and are conducted at the Beijing Createch Testing Technology Co., Ltd., P. R. China.

Fluid inclusion microthermometry

Petrography of fluid inclusions are studied using optical microscopy, the classification and recognition criteria of primary fluid inclusions by Roedder[30] and Lu et al.[31] are applied. Linkam-THMSG 600 cooling-heating stage with an operating temperature range of − 195 to 600 °C is used for microthermometry, and is calibrated by international synthetic fluid inclusion standard. The temperature stabilities are ± 0.1 °C, ± 1 °C and ± 2 °C between − 195 to 30 °C, 30 to 300 °C and 300 to 600 °C, respectively. The salinities of H_2O-NaCl fluid inclusions are calculated based on the freezing point-salinity equation[32]. The salinities of halite daughter mineral-bearing fluid inclusions are calculated using the halite final melting temperature-salinity equation[31,33]. The salinities of CO_2-bearing fluid inclusions are calculated using the melting temperatures of clathrate[34]. Gas- and solid-phase composition analysis of individual fluid inclusions is performed by using a Renishaw inVia reflex Laser Raman spectrometer, the laser power is 20 MW, the wavelength of the argon ion laser is 514 nm and the laser spot size is 1 μm, the scanning range is 120 to 4200 cm^{-1}, the scanning time is 30 to 60 s, and the experimental temperature is controlled at 23 °C.

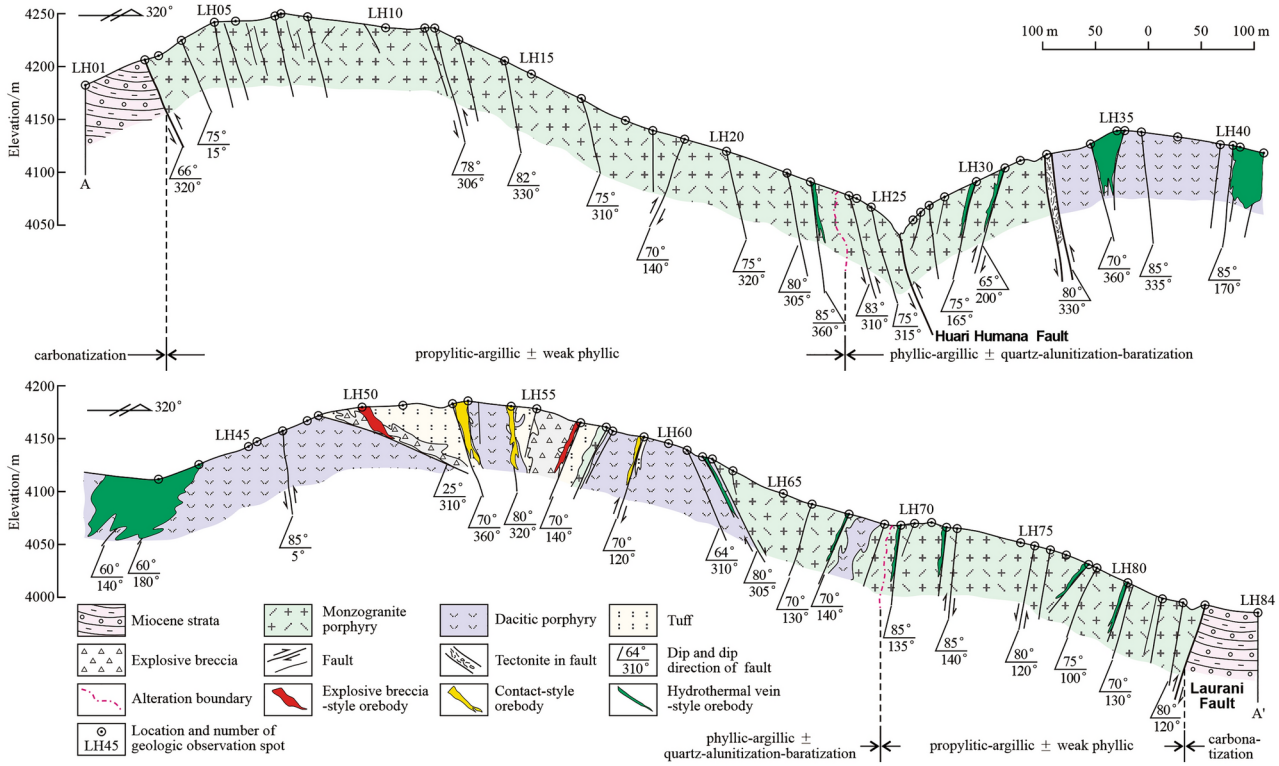

Fig. 3. The A–A′ comprehensive geological profile in the Laurani deposit (modified after Liu et al.[19]). The position is shown in Fig. 2. The upper part is the SE segment, and the lower part is the NW segment.

Hydrogen and oxygen isotope analysis

All the samples are cleaned and remove the absorbed water. Oxygen isotope analysis of pure quartz is performed by the BrF_5 method to produce O that reacted with BrF_5 at 550–630 °C, and then converted to CO_2 on a platinum-coated carbon rod at 700 °C[35]. Oxygen isotope analysis of barite is performed using the pyrolysis method, CO is produced by combustion pyrolysis in a graphite furnace at 1450 °C, and helium gas is used as a carrier gas and different gases are separated by a chromatographic column, then is measured in a continuous flow mode. Hydrogen isotope analysis is also performed by the pyrolysis method, the inclusion water in quartz and barite grains is released by pyrolysis and is reacted with vitreous carbon instantaneously at 1380 °C to generate H_2 and CO, helium gas is used as a carrier gas, and different gases are separated by a chromatographic column. The H-O isotope analysis is conducted on a MAT 253 plus mass spectrometer, with analytical precisions are better than ± 0.2‰ and ± 1‰ for O and H isotopes, respectively. The resulting values are given in $\delta^{18}O$ and δD values relative to the V-SMOW.

Sulfur and lead isotope analysis

The sulfur isotope analysis utilizes the processed product of SO_2 that through a reaction with Cu powder[36], after collecting and purifying, the sulfur isotope of SO_2 is measured by using a MAT 253 plus mass spectrometer. The results are reported as $\delta^{34}S_{VCDT}$ with a precision better than ± 0.2‰.

For the lead isotope analysis, processed samples are fully dissolved in an ultrapure concentrated acid mixture of HF and HNO_3 (2:1), separation and purification of the Pb isotope is performed using strontium selective specific resin. The Pb isotopic values are analyzed by Neptune plus type MC-ICP-MS. The concentration of Pb in the solution is verified, and a standard solution of Tl is added to make Pb:Tl = 1:1. The fractionation correction of the isotope instrument use an exponential equation subjected to $^{203}Tl/^{205}Tl = 0.418922$.

Results

Fluid inclusion

Fluid inclusion petrography

Fluid inclusions develop well in the selected minerals (Fig. 7), while melt inclusions, secondary inclusions, and pseudosecondary inclusions can be observed. Most fluid inclusions present randomly clustered or isolated, indicating they belong to primary inclusions in origin[31], which are focused on in this study. Based on the composition and the phase relations observed at room temperature[30,31], four types of fluid inclusions have been identified at Laurani: pure liquid aqueous inclusions (type I), vapor–liquid two-phase aqueous inclusions (type II), CO_2-bearing three-phase inclusions (type III) and daughter mineral-bearing inclusions (type IV). The type I inclusions only involve a single liquid phase, are mainly formed in the stage II quartz veins and barite veins (Fig. 7h), and occur occasionally in the stage II quartz eyes (Fig. 7n). They usually distribute in clusters or as

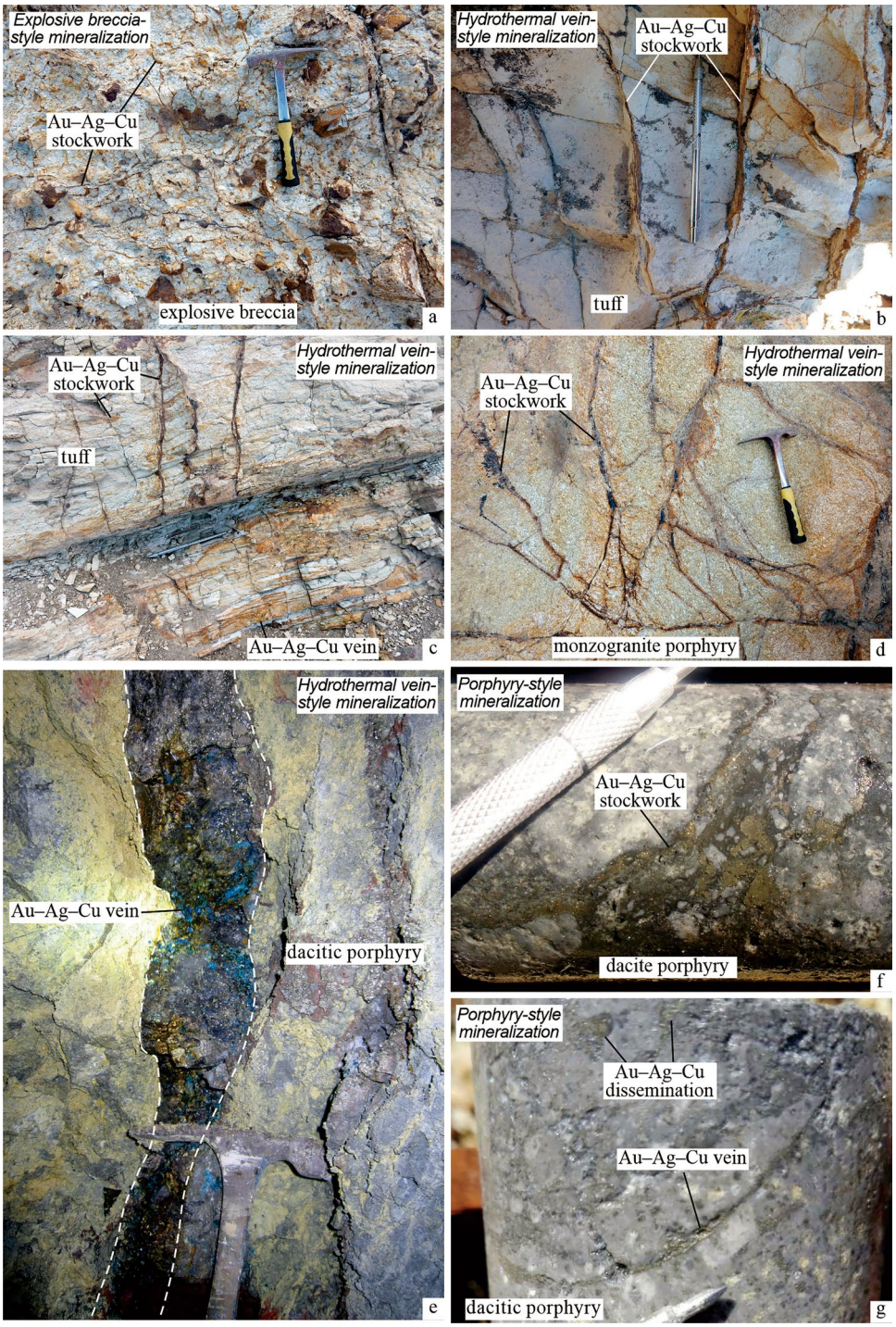

Fig. 4. Characteristics of mineralization style in the Laurani deposit. (**a**) shows explosive breccia-style Au–Cu orebodies, (**b**–**e**) show hydrothermal vein-style Au–Ag–Cu–Pb–Zn orebodies and (**f**,**g**) show porphyry-style Au–Cu orebodies.

isolated forms, with many exhibiting elongated axial, oval, and regular polygonal shapes. Their sizes range from 1 to 26 μm, and they frequently coexist with the type II and IV inclusions (Fig. 7h,n). The type II inclusions contain both liquid and vapor phases and develop in all selected minerals (Fig. 7). They usually appear in clusters or as isolated forms, exhibiting various shapes of oval, negative-crystal and irregular polygonal forms, with sizes ranging from 1 to 40 μm. Based on phase state and filling degrees, the type II inclusions are further divided in two subtypes: type II-a (liquid-rich aqueous inclusions) and type II-b (vapor-rich aqueous inclusions). The former is well developed in the stage II quartz veins, barite veins and quartz eyes, and the stage III sphalerite, they are homogenized to the liquid phase. The latter is less developed than the type II-a inclusions, occurs

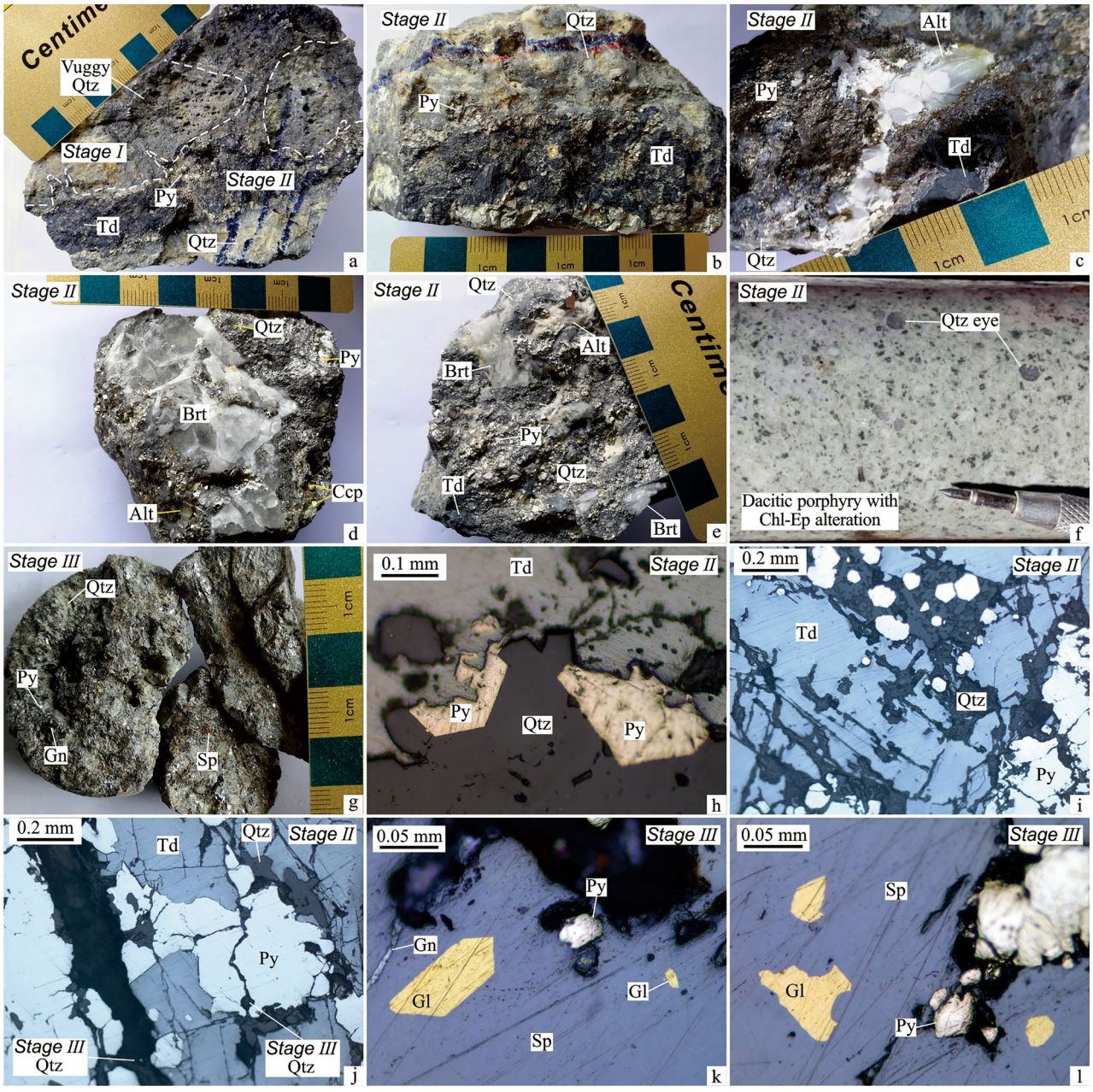

Fig. 5. Characteristic of ores from different mineralization (hydrothermal) stages in the Laurani deposit. (**a**) The stage I ore-barren vuggy quartz vein is cut by the stage II quartz + tetrahedrite + pyrite vein; (**b**) The stage II pyrite + tetrahedrite + quartz vein; (**c**) The stage II pyrite + tetrahedrite + quartz + alunite vein; (**d**) The stage II pyrite + quartz + alunite + barite vein, containing a few of disseminated chalcopyrite; (**e**) The stage II pyrite + tetrahedrite + quartz + alunite + barite vein; (**f**) Quartz eyes develop in the dacitic porphyry with chlorite + epidote + (quartz) alteration halo, these quartz eyes are mainly observed with or nearly with the porphyry-style mineralization from the stage II in the depth; (**g**) The stage III galena + sphalerite + pyrite vein, with scarce quartz; (**h**) Microphotography of the stage II pyrite + tetrahedrite + quartz vein; pyrite exists idiomorphic-hypautomorphic granular texture, tetrahedrite exists xenomorphic granular texture, quartz contains and replaces pyrite and tetrahedrite, showing a dominant paragenetic relationship; (**i**) Microphotography of the stage II pyrite + tetrahedrite + quartz vein; pyrite exists idiomorphic-hypautomorphic granular texture, pyrite is intergrowth with tetrahedrite and quartz to form common edge texture, showing a paragenetic relationship; (**j**) Microphotography of the stage II pyrite + tetrahedrite + quartz vein is cut by the stage III quartz vein; (**k**) Microphotography of the stage III galena + sphalerite + pyrite vein; gold exists idiomorphic-hypautomorphic granular texture, sphalerite contains pyrite and gold to form poikilitic texture; (**l**) Microphotography of the stage III sphalerite + pyrite vein, sphalerite contains pyrite and gold to form poikilitic texture. Qtz = quartz, Alt = alunite, Brt = barite, Chl = chlorite, Ep = epidote, Py = pyrite, Td = tetrahedrite, Ccp = chalcopyrite, Gn = galena, Sp = sphalerite, Gl = gold.

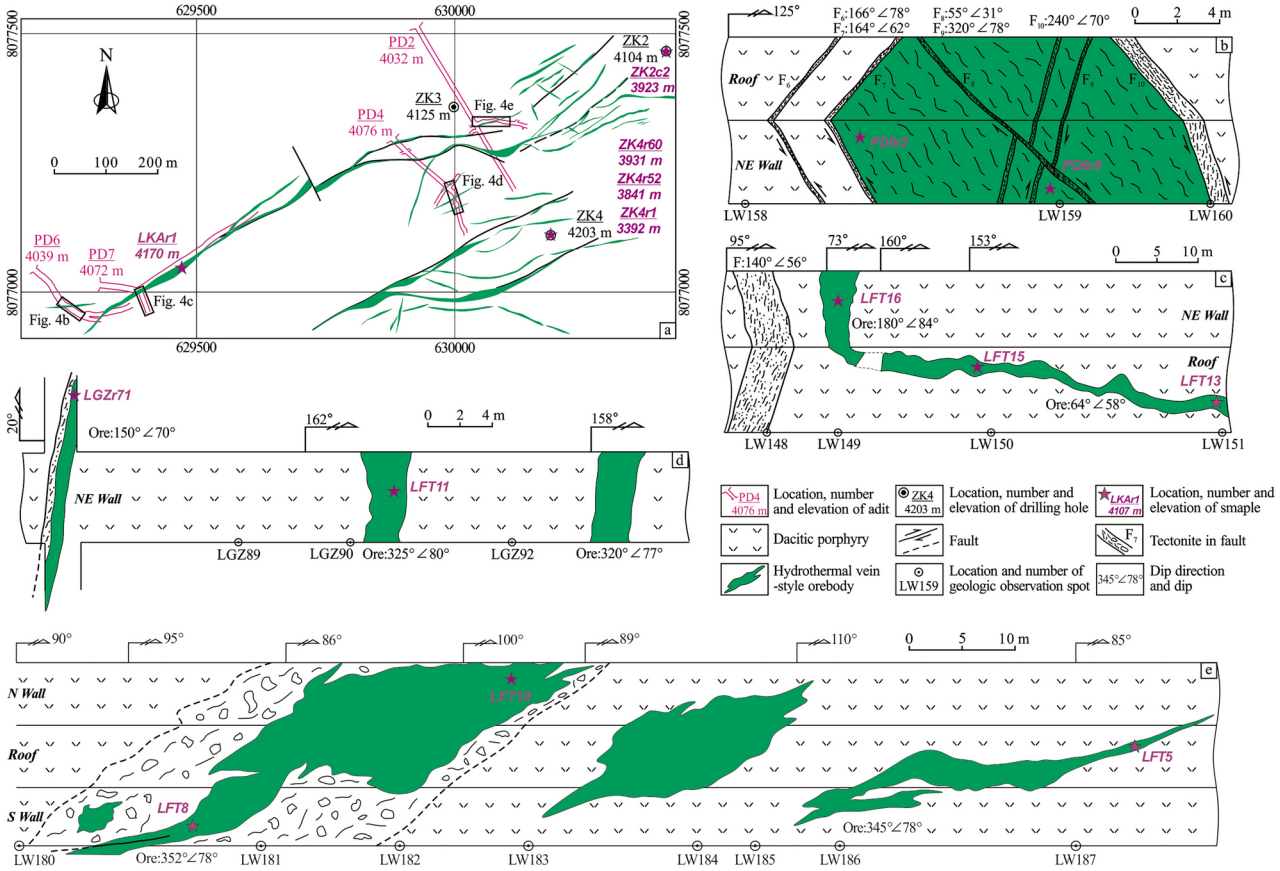

Fig. 6. The specific locations of analyzed samples.

mainly in the stage II quartz veins and barite veins, and commonly coexists with the type I and II-a inclusions. These inclusions are homogenized to the vapor phase. The type III inclusions are rarely and mainly observed in the stage II quartz veins and the stage III sphalerite (Fig. 7f,l). They comprise an aqueous phase and two carbon dioxide phases of liquid and vapor, ranging in size from 2 to 30 μm. These inclusions typically coexist with the type I and II-a inclusions. The type IV inclusions are commonly found in the stage II quartz veins, barite veins and quartz eyes (Fig. 7), with vapor, liquid and solid phases coexisted and range in size from 2 up to 60 μm, generally occurring with the type I and II-a inclusions.

Microthermometric results

The microthermometric results are summarized in Table 1 and Fig. 8, the raw data of microthermometry can been found in supplementary Table A.

In the stage I ore-barren quartz, the type II-a inclusions yield ice-melting and homogenization temperatures from − 19.8 to − 0.1 °C and 164 to 397 °C, respectively, with salinities of 0.2–22.2 wt.% $NaCl_{eq}$ (Table 1). Ice-melting and homogenization temperatures from two type II-b inclusions are − 7.2 to − 1.4 °C and 411 to 451 °C, respectively, with salinities of 2.4–10.7 wt.% $NaCl_{eq}$ (Table 1). For the type III inclusions, the carbonic phase melt at − 64.9 to − 59.4 °C ($T_{m,\ CO2}$), the melting temperature of CO_2 clathrate ($T_{m,\ cla}$) and partial homogenization temperature ($T_{h,\ CO2}$) are 7.0–8.8 °C and 24.3–28.4 °C, respectively, with salinities of 2.4–5.7 wt.% $NaCl_{eq}$, and the total homogenization temperature occur at 317–404 °C (Table 1). Two type IV inclusions (daughter minerals are calcite) yield ice-melting and homogenization temperatures of − 21.0 to − 20.5 °C and 277 to 304 °C, respectively, with salinities from 22.7 to 23.1 wt.% $NaCl_{eq}$ (Table 1).

In the stage II tetrahedrite + pyrite + quartz ± barite ± alunite ores, the type II-a inclusions from quartz eyes, quartz veins and barite veins are homogenized at 146–397 °C, with ice-melting temperatures from − 20.3 to − 0.2 °C and salinities of 0.4–22.4 wt.% $NaCl_{eq}$ (Table 1). One type II-b inclusion from barite vein yields an ice-melting temperature of − 11.2 °C and homogenization temperature of 313 °C, with a salinity of 15.2 wt.% $NaCl_{eq}$ (Table 1). The type IV inclusions (daughter minerals are calcite or sulfide) from quartz vein yield ice-melting and homogenization temperatures ranging from − 5.2 to − 1.6 °C and 215 to 262 °C, respectively, with salinities from 2.7 to 8.1 wt.% $NaCl_{eq}$ (Table 1). In addition, the homogenization temperatures of type IV inclusions from quartz eyes give values between 241 to 261 °C, with halite final melt temperatures variable from 346 to 450 °C and salinities from 42.1 to 53.3 wt.% $NaCl_{eq}$ (Table 1).

The type II-a inclusions of sphalerite from the stage III yield ice-melting temperatures of − 4.3 to − 2.5 °C, with salinities of 4.2–6.9 wt.% $NaCl_{eq}$ and homogenization temperatures of 193–249 °C (Table 1).

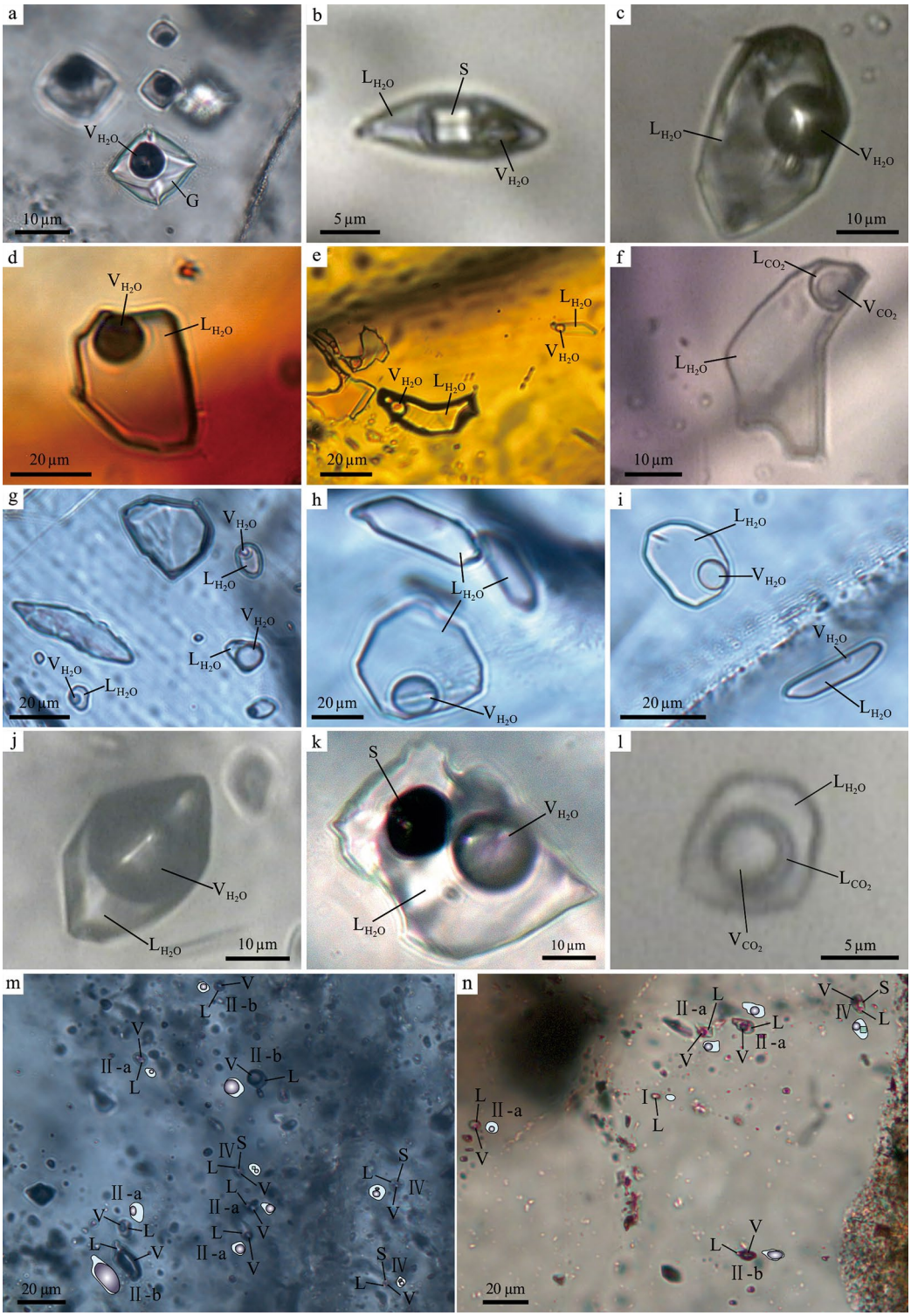

Fig. 7. Characteristics of fluid inclusion within quartz, barite and sphalerite in the Laurani deposit. (**a**) Melt inclusions in the stage II quartz eye (sample ZK4r52); (**b**) Daughter mineral-bearing inclusion in the stage II quartz eye (sample ZK4r1); (**c**) Liquid-rich aqueous inclusion in the stage II quartz eye (sample ZK4r1); (**d**,**e**) Liquid-rich aqueous inclusion in the stage III sphalerite (sample ZK2c2); (**f**) CO_2-bearing three-phase inclusion in the stage III sphalerite (sample ZK2c2); (**g**–**i**) Pure liquid aqueous, vapor-rich and liquid-rich aqueous inclusion in the stage II barite vein (sample ZK4r60 and LET15); (**j**) Vapor-rich aqueous inclusion in the stage II quartz vein (sample LET11); (**k**) Daughter mineral-bearing inclusion in the stage II quartz vein (sample PD6r2); (**l**) CO_2-bearing three-phase inclusion in the stage I ore-barren quartz (sample LET16); (**m**,**n**) Vapor-rich, liquid-rich, and daughter mineral-bearing inclusions in the same viewshed in the stage I ore-barren quartz (sample LET16) and of the stage II quartz eyes (sample ZK4r1). All images are observed in plane polarized light. G-glass, V-vapor, L-liquid, S-solid.

Mineralization stage	Host mineral	Fluid inclusion types	$T_{m, ice}$	$T_{m, CO2}$	$T_{m, cla}$	$T_{h, CO2}$	$T_{m, hal}$	T_h	Salinity
Stage I	Ore-barren quartz	II-a	− 19.8 to − 0.1	–	–	–	–	164 to 397 (33)	0.2 to 22.2
		II-b	− 7.2 to − 1.4	–	–	–	–	411 to 451 (2)	2.4 to 10.7
		III	–	− 64.9 to − 59.4	7.0 to 8.8	24.3 to 28.4	–	317 to 404 (3)	2.4 to 5.7
		IV	− 21.0 to − 20.5	–	–	–	calcite	277 to 304 (2)	22.7 to 23.1
Stage II	Quartz vein	II-a	− 7.8 to − 0.2	–	–	–	–	146 to 278 (99)	0.4 to 11.2
		IV	− 5.2 to − 1.6	–	–	–	calcite/sulfide	215 to 262 (7)	2.7 to 8.1
	Quartz eye	II-a	− 20.3 to − 0.3	–	–	–	–	222 to 353 (33)	0.5 to 22.4
		IV	–	–	–	–	Halite, 346–450	241 to 261 (4)	42.1 to 53.3
	Barite vein	II-a	− 12.8 to − 0.4	–	–	–	–	149 to 397 (136)	0.7 to 16.7
		II-b	− 11.2	–	–	–	–	313 (1)	15.2
Stage III	Sphalerite	II-a	− 4.3 to − 2.5	–	–	–	–	193 to 249 (26)	4.2 to 6.9

Table 1. The summary of microthermometric data of fluid inclusions in the Laurani deposit. All temperatures in °C. $T_{m, ice}$ = final melting temperature of ice; $T_{m, CO2}$ = melting temperature of the carbonic phase; $T_{m, cla}$ = melting temperature of the CO_2 clathrate; $T_{h, CO2}$ = partial homogenization temperature of carbonic inclusion; $T_{m, hal}$ = final melting temperature of halite crystal; T_h = total homogenization temperature. Salinity expressed as wt.% NaCl equivalent. The numbers in brackets represent the numbers of fluid inclusions measured.

Raman spectroscopy

The type II, type III, and type IV fluid inclusions from the stage I vuggy quartz, the stage II quartz veins and barite veins, and the stage III sphalerite are analyzed for Raman spectroscopy. It reveals that the vapor phases in the Laurani deposit are dominantly H_2O, with a little CO_2, and traces N_2 and CH_4 (Fig. 9). In addition to halite, daughter minerals (solid phases) include some calcites and pyrites as well (Fig. 9).

Hydrogen and oxygen isotope

The measured hydrogen and oxygen isotopic values at Laurani and those collected for plotting Fig. 10 are listed in supplementary Table B. O isotopes of hydrothermal solutions are calculated by utilizing the equation of the measured $\delta^{18}O$ values and the corresponding experimented fluid inclusion homogenization temperatures in the hosted minerals of quartz and barite from Clayton et al.[37] and Kusakabe and Robinson[38], respectively. The early stage I ore-barren quartz exhibits relatively high $\delta^{18}O_{H2O}$ values of 9.52 to 12.27‰ and moderate δD values of − 72.70 to − 71.57‰ (Table 2). Quartz vein and barite vein from the stage II show lower $\delta^{18}O_{H2O}$ values from 5.66 to 10.99‰ and various δD values from − 101.50 to − 41.31‰ (Table 2).

Sulfur and lead isotope

The sulfur isotopes at Laurani and those collected for plotting Fig. 11 are listed in supplementary Table C. The S isotopic data at Laurani are summarized in Table 3. Pyrites and tetrahedrites from the stage II have $\delta^{34}S$ values of 1.57–3.66‰, while the paragenetic barites have relatively high $\delta^{34}S$ values of 24.01 to 25.90‰ (Table 3). Galena and sphalerite from the stage III have $\delta^{34}S$ values of 3.26–5.55‰ (Table 3).

The lead isotopes from the Laurani ores and those collected for plotting Fig. 12 are listed in supplementary Table D. The Pb isotopic compositions at Laurani are summarized in Table 4. It shows a concentrated Pb isotopes, with $^{206}Pb/^{204}Pb = 18.2869–18.3568$, $^{207}Pb/^{204}Pb = 15.6082–15.6337$, and $^{208}Pb/^{204}Pb = 38.6937–38.7719$ (Table 4). The Pb model ages (T), and two parameters of μ ($^{238}U/^{204}Pb$) and κ ($^{232}Th/^{238}U$) are calculated based on Faure[39], showing the Pb model ages between 231 and 280 Ma, $\mu = 9.49–9.54$ and $\kappa = 3.88–3.91$ (Table 4).

Discussion

Mineralization and alteration characteristics

The high-sulfidation epithermal deposits vary in forms of disseminations or replacements to veins, stockworks, and hydrothermal breccia bodies[3]. Similarly, four styles of explosive breccia Au–Cu, contact Cu–Au–Ag, hydrothermal vein Au–Ag–Cu–Pb–Zn, and porphyry Au–Cu mineralization are developed in the Laurani high-sulfidation epithermal deposits (Fig. 4). As previously mentioned, these individual mineralization styles at Laurani are controlled predominantly by lithologies and structures, which is similar to the most high-sulfidation epithermal deposits in the world[8].

At Laurani, hydrothermal alterations are well developed and exhibit significant zonation[16] (Fig. 3). Vuggy and/or massive quartz is common, in combination with alunite, kaolinite and/or dickite, indicating that the initial fluids causing alteration and rock dissolution are extremely acid[7,8]. Vuggy quartz predates metal deposition, illustrating the importance of paleo-permeability in preparation for metal deposition[8,40]. Quartz, alunite and barite commonly accompany high-sulfidation sulfide orebodies, the presence of magmatic hydrothermal alunite reflects the fluids are relatively oxidized[8], and barite is an insoluble gangue mineral that remains even after complete oxidation of sulfides[3]. Besides, quartz eyes[41] can be widely observed in the Laurani deposit (Fig. 5f), containing the single-phase pure liquid aqueous inclusions, vapor–liquid two-phase aqueous inclusions, and daughter mineral-bearing inclusions (Fig. 7b,c,n) as well as melt inclusions (Fig. 7a), which are similar to the studies by Vasyukova et al.[41] in porphyry deposits. And the abundant occurrence of quartz eyes may be significant

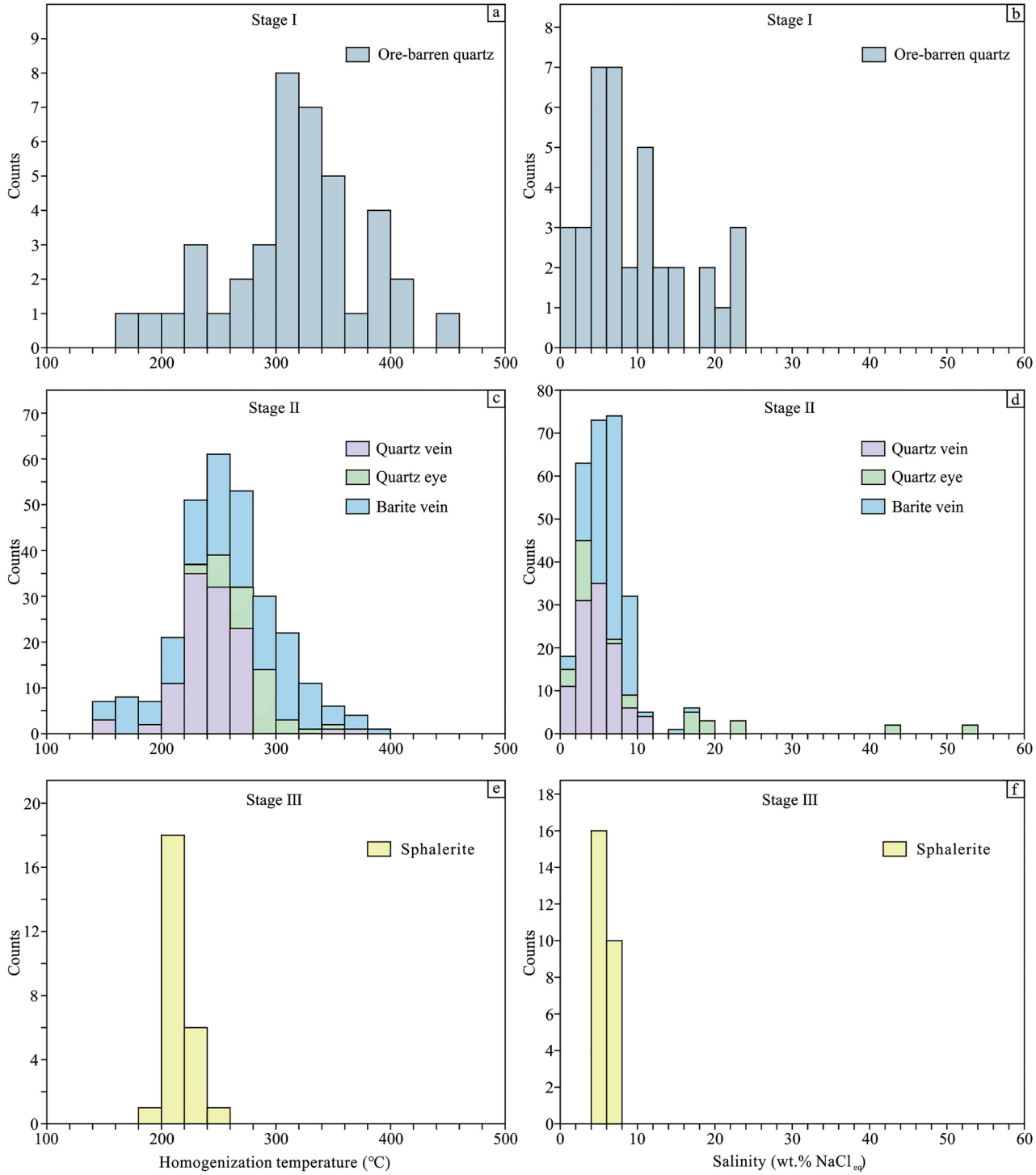

Fig. 8. Homogenization temperature and salinity of fluid inclusions from different mineralization stages in the Laurani deposit.

evidence of large-scale fluid exsolution[42]. However, potassic zone is absent in the Laurani deposit, which may be owing to its possible existence in deep and has not been revealed[16]. In conclusion, the characteristics of hydrothermal alterations and alteration zonation at Laurani are consistent with those polymetallic veins and high-sulfidation epithermal systems related to porphyry system at depth[8–11,40].

Sources of ore-forming fluids

H–O isotopes of ore-forming fluids from the high-sulfidation epithermal deposits typically show trends that extend from magmatic compositions to the meteoric water line, with many values closer to the magmatic end[7,8,43]. At Laurani, the ore-forming fluids from both the stage I ore-barren quartz and the stage II quartz vein

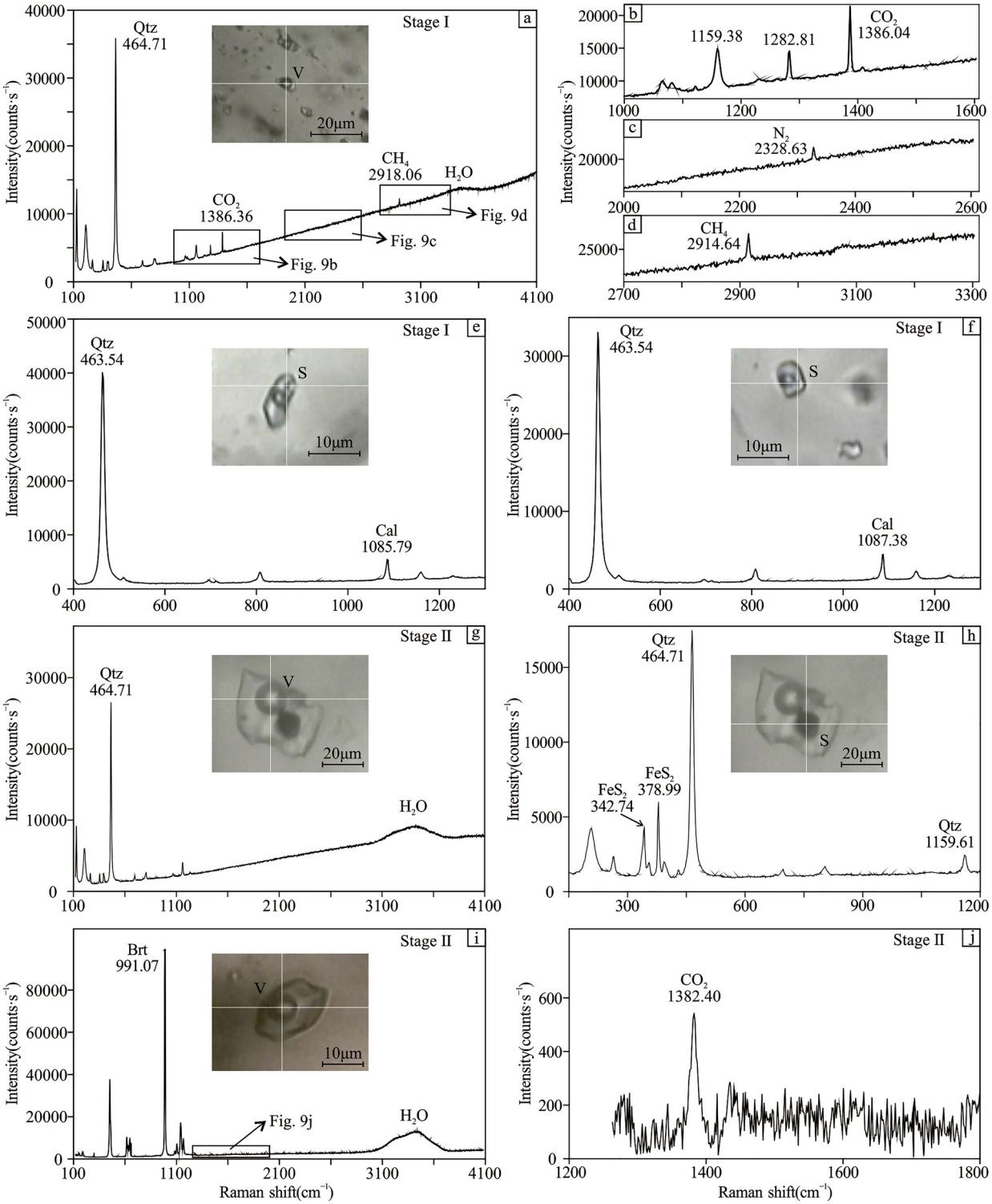

Fig. 9. Laser raman spectra of fluid in the Laurani deposit. Qtz = quartz, Cal = calcite, Brt = barite, V-vapor, S-solid.

and barite vein have a relatively concentrated values of δD (−101.50 to −60.80‰) and $\delta^{18}O_{H2O}$ (6.00 to 12.27‰), except for one outlier value of $\delta D = -41.31$‰ and $\delta^{18}O_{H2O} = 5.66$‰ of quartz vein from the stage II (Table 2; Fig. 10). The H–O isotopic values in the Laurani deposit coincide with those of primary magmatic water[44], and also show remarkable trend that extend from primary magmatic water to the meteoric water line and with a lot distribute in the magmatic end (Fig. 10), indicating the ore-forming fluids are mainly a magmatic source. Most of δD and $\delta^{18}O_{H2O}$ values from the stage II quartz vein and barite vein are lower than those from the stage I ore-barren quartz and are closer to meteoric water line (Table 2; Fig. 10), reflecting meteoric water may mainly

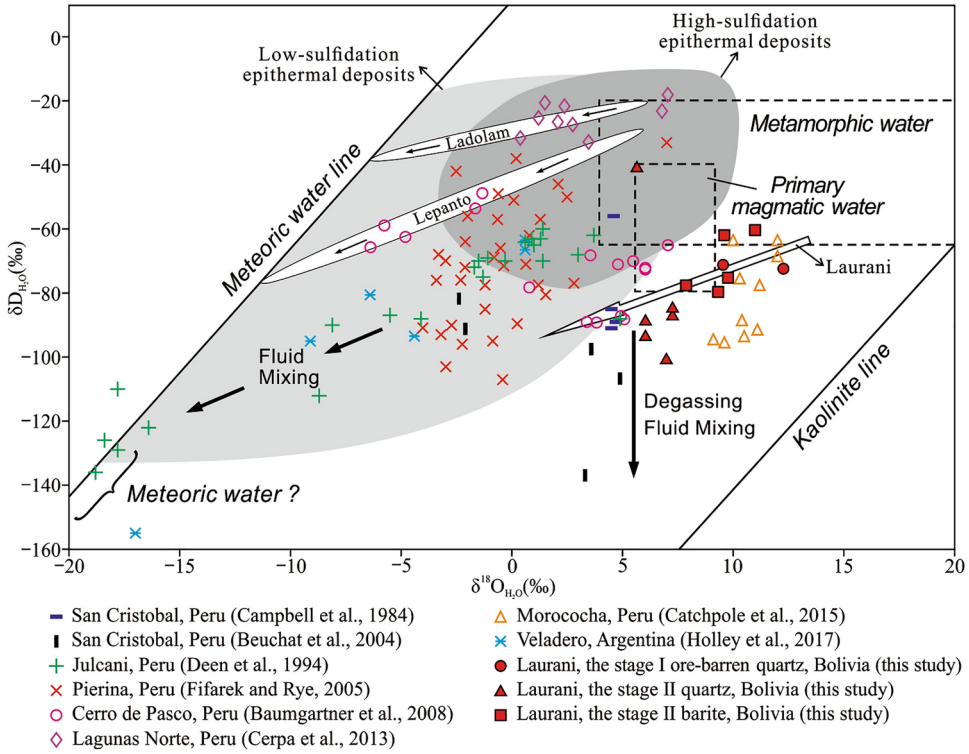

Fig. 10. Hydrogen and oxygen isotopic compositions of late Miocene epithermal deposits in the central Andes. Hydrogen and oxygen isotope data are taken from Campbell et al[82], Deen et al.[48], Beuchat et al.[49], Fifarek and Rye[51], Baumgartner et al.[52], Cerpa et al.[53], Catchpole et al.[54], Holley et al.[55] and this study (for Laurani deposit). Isotopic compositions of high- and low-sulfidation epithermal deposit, and trend for Lepanto and Ladolam are modified after Simmons et al[8]. Meteoric water line, and metamorphic and primary magmatic water are based on Taylor[44]. Kaolinite line is based on Savin and Epstein[83].

Mineralization stage	Sample NO	Minerals	$\delta D_{V\text{-}SMOW}$ (‰)	$\delta^{18}O_{V\text{-}SMOW}$ (‰)	Temperature (℃)	$\delta^{18}O_{H2O}$(‰)
Stage I	LKAr1	Ore-barren quartz	−71.57	16.49	312 (18)	9.52
	LFT16	Ore-barren quartz	−72.70	19.01	319 (22)	12.27
Stage II	LFT13	Quartz vein	−101.50	17.41	230 (21)	6.96
	LFT11	Quartz vein	−87.53	17.02	243 (20)	7.24
	LFT5	Quartz vein	−41.31	15.90	234 (20)	5.66
	PD6r5	Quartz vein	−89.19	15.91	241 (7)	6.02
	PD6r2	Quartz vein	−85.38	16.44	256 (25)	7.27
	LGZr71	Quartz vein	−94.16	16.56	228 (13)	6.00
	ZK4r60	Barite vein	−62.37	12.48	271 (28)	9.61
	LFT15	Barite vein	−75.54	13.38	251 (35)	9.73
	LFT11	Barite vein	−78.18	10.89	267 (19)	7.88
	LFT10	Barite vein	−60.80	13.64	277 (28)	10.99
	LFT8	Barite vein	−79.93	12.63	259 (27)	9.30

Table 2. Hydrogen and oxygen isotopic compositions in the Laurani deposit. The numbers in brackets represent the numbers of measured fluid inclusions.

enter into the ore-forming system in the stage II. This is consistent with the similar source of the ore-forming fluids that a majority of magmatic water mixing with meteoric water, which is typically for the high-sulfidation epithermal deposits[8,43], as well as for many porphyry-type copper deposits (PCDs) worldwide[45–47]. Therefore, we suggest that the ore-forming fluids of the Laurani high-sulfidation epithermal deposit are primarily derived from magmatic water, mixing with a little meteoric water.

Furthermore, similar to the Laurani deposit, the H–O isotopic compositions of some Miocene high-sulfidation epithermal deposits from the Central Andes also indicate a predominantly magmatic component with a minor meteoric water presence in the ore-forming fluids[48–55] (Fig. 10).

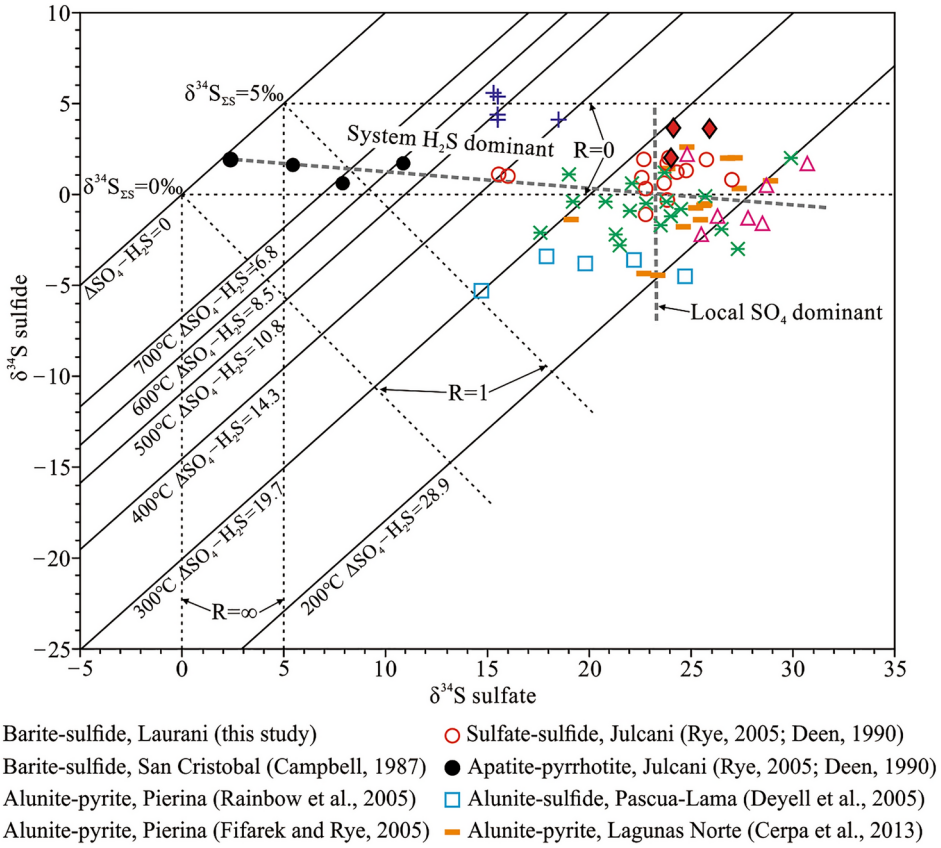

Fig. 11. Sulfur isotopic compositions of the late Miocene epithermal deposits in the central Andes. Sulfur isotope data are taken from Campbell[84], Deen[66], Deyell et al.[50], Fifarek and Rye[51], Rainbow et al.[85], Rye[61], Cerpa et al.[53] and this study (for Laurani deposit; the three stage II barite-sulfide pairs from the samples ZK4R60, LFT5 with LFT10, and LFT13 with LFT15 in Table 3, the last two sample pairs are taken from the two same orebodies, respectively). The original diagram is modified after Rye[61]. The nearly horizontal line through the hydrothermal and igneous data reflects a combination of disequilibrium in the igneous system and late hydrothermal systems and the average equilibrium values for magmatic-hydrothermal alunite in an overall H_2S-dominant system[61]; the near-vertical line represents the local shift to a SO^{2-}_4-dominant system during acid sulfate alteration[61]. R is defined in terms of SO^{2-}_4/H_2S[61].

Mineralization stage	Sample No	Minerals	$\delta^{34}S_{V\text{-}CDT}$(‰)
Stage II	PD6r2	Pyrite	2.46
	LFT5	Pyrite	3.66
	LFT13	Tetrahedrite	3.62
	PD7r1	Tetrahedrite	2.26
	LGZr71	Tetrahedrite	1.57
	ZK4r60	Tetrahedrite	2.02
	ZK4r60	Barite	24.01
	LFT15	Barite	25.90
	LFT10	Barite	24.13
Stage III	ZK2c2	Galena	3.26
	ZK2c2	Sphalerite	5.55

Table 3. Sulfur isotopic compositions of sulfides and sulfates in the Laurani deposit.

Evolution of ore-forming fluids

At Laurani, the fluid inclusion microthermometric results from the stage I ore-barren quartz indicate the existence of low- to moderate-salinity (primarily 0.2–13.0 wt.% $NaCl_{eq}$), high-temperature (mostly higher than 300 ℃) and CO_2-bearing fluids (Table 1; Fig. 8). They dovetail with the early leaching fluids that condensed from magmatic vapor[7] and the silica-alunite stage fluids summarized by Henley and Berger[56] that with a high

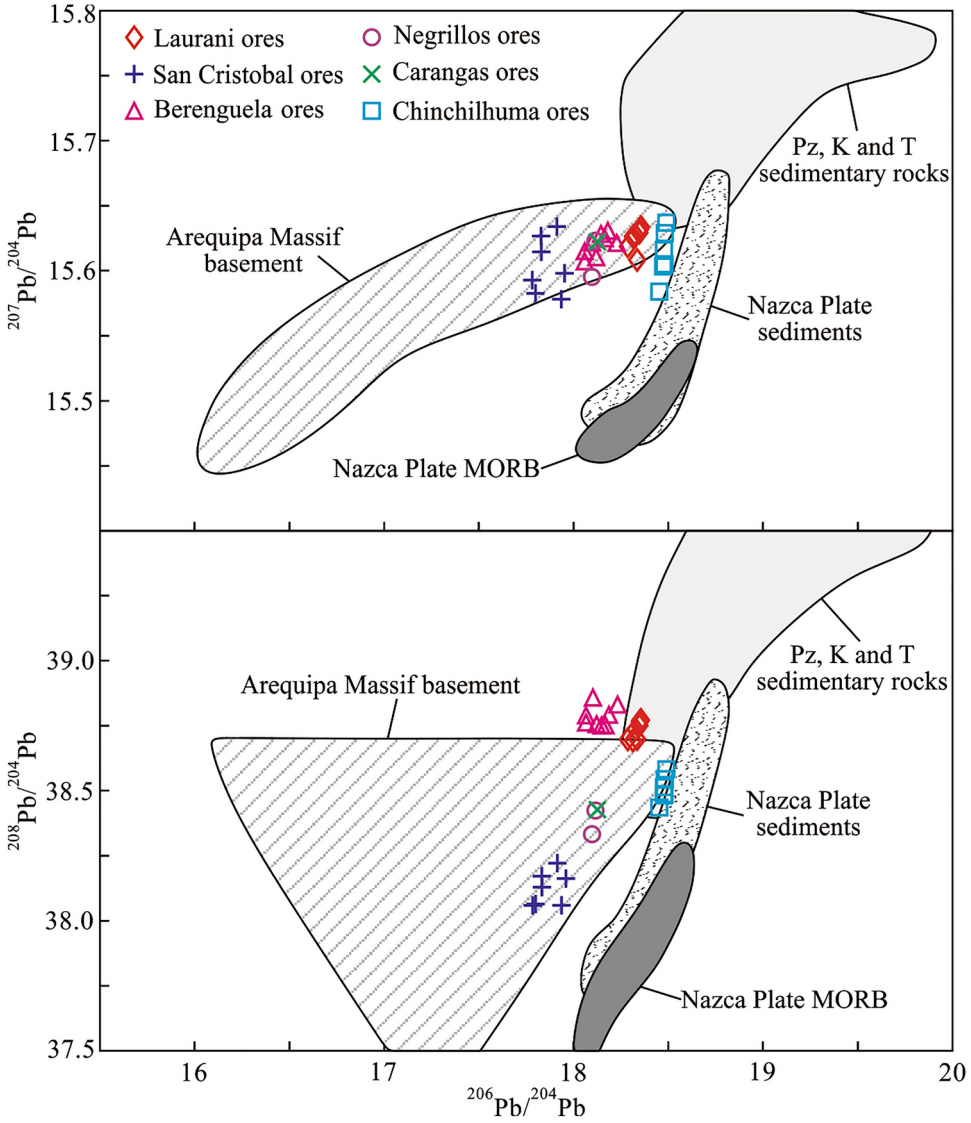

Fig. 12. Lead isotopic compositions of ores from the late Miocene epithermal deposits in the central Andes (between about 16°–21°S), compared with potential metal sources. Lead isotope data of ores are taken from Kamenov et al.[60], Macfarlane and Lechtman[71] and this study (for Laurani deposit). Lead isotopic compositions of Nazca Plate MORB, Nazca Plate sediments and Pz, K and T sedimentary rocks are drawn from Kamenov et al.[60]; Lead isotopic compositions of Arequipa Massif basement are based on Mamani et al.[67] and Ramos[68], in the plot of $^{207}Pb/^{204}Pb$ vs. $^{206}Pb/^{204}Pb$ modified from Ramos[68], in the plot of $^{208}Pb/^{204}Pb$ vs. $^{206}Pb/^{204}Pb$ modified from Macfarlane and Lechtman[71], whose $^{208}Pb/^{204}Pb$ ratios are higher than those of Mamani et al.[67] and Ramos[68].

Mineralization stage	Sample no	Minerals	$^{206}Pb/^{204}Pb$	$^{207}Pb/^{204}Pb$	$^{208}Pb/^{204}Pb$	*T*/Ma	$^{238}U/^{204}Pb$ (μ)	$^{232}Th/^{238}U$ (κ)
Stage II	PD6r2	Pyrite	18.3568	15.6337	38.7719	247	9.54	3.91
	LFT5	Pyrite	18.3139	15.6262	38.6937	269	9.53	3.90
	LFT13	Tetrahedrite	18.3281	15.6272	38.7362	260	9.53	3.91
	PD7r1	Tetrahedrite	18.2869	15.6188	38.6970	280	9.51	3.91
	LGZr71	Tetrahedrite	18.3487	15.6295	38.7503	248	9.53	3.90
	ZK4r60	Tetrahedrite	18.3362	15.6082	38.6989	231	9.49	3.88
Stage III	ZK2c2	Galena	18.3518	15.6325	38.7706	250	9.53	3.91
	ZK2c2	Sphalerite	18.3493	15.6319	38.7651	251	9.53	3.91

Table 4. Lead isotopic compositions of sulfides in the Laurani deposit.

temperature (> 500 ℃) and wide range of temperatures, which reflect the properties of the initial ore-forming fluids that derived from magmatic water in the porphyry–epithermal metallogenic system[43,45,57–59]. In the stage I ore-barren quartz, the daughter mineral-bearing inclusions, liquid- and vapor-rich aqueous inclusions can be observed in the same viewshed (Fig. 7m), and these fluid inclusions yield homogenization temperatures of 265–357 ℃ with salinity varied from ~ 2 to 23 wt.% $NaCl_{eq}$, suggesting fluid boiling occurs from about 260 to 360 ℃. The variations of salinity without temperature change caused by fluid boiling, which is one of the important mechanisms promoting mineral precipitation and occurs commonly in many porphyry–epithermal deposits, such as Shizitou porphyry Mo deposit[45], Morococha district[54] and Cerro de Pasco epithermal polymetallic deposit[52].

In the stage II tetrahedrite + pyrite + quartz ± barite ± alunite veins, the microthermometric results obtained from the stage II quartz eyes are characterized by three distinctive salinities of 0.5–9.9 wt.%, 17.3–22.4 wt.% and 42.1–53.3 wt.% $NaCl_{eq}$ (Table 1; Fig. 8). The variations in salinity are mainly owing to the boiling of fluids, which can be confirmed by the boiling inclusion group that the pure liquid aqueous inclusions, the liquid- and vapor-rich aqueous inclusions and the daughter mineral-bearing inclusions generated together in the same place (Fig. 7n). These inclusions yield the temperatures of 247–352 ℃, indicating fluid boiling takes place at ~ 250 to 350 ℃, which like those occur in the stage I ore-barren quartz. The homogenization temperatures obtained from the stage II quartz veins are relatively narrow, most of them are 200 to 280 ℃, with low- to moderate-salinity of 0.4–11.2 wt.% $NaCl_{eq}$. Compared to quartz veins, the homogenization temperatures of the stage II barite veins show a wide range and decreasing trend from 397 to 146 ℃, while the salinities have a narrow range from 0.7 to 10.7 wt.% $NaCl_{eq}$ except for two greater than 15 wt.% $NaCl_{eq}$ and show a decreasing trend as well (Fig. 13). These features coincide with low salinities that less than 5 wt.% $NaCl_{eq}$ and a wide range of homogenization temperatures of 150–300 °C of ore-forming fluids in sulfide stage[56]. The decrease in temperatures and salinities is reasonably interpreted as decompression caused by structural activity, and/or as cooling resulted from mixing with meteoric water that also confirmed by the H–O isotopic results (Fig. 10). Furthermore, the homogenization temperatures and salinities obtained from sphalerite in the stage III veins are relatively low (Table 1; Fig. 8), representing the properties of the late-stage evolved ore-forming fluids.

In summary, the evolution of ore-forming fluids at Laurani mainly involves three processes (Fig. 13): (1) boiling, which occurs at about 250 to 360 ℃, causing the loss of CO_2 and an increase in salinity, then inducing the formation of some daughter mineral-bearing inclusions of halite and/or calcite, which generate mainly in shallower parts relative to halite because of boiling and loss of CO_2 not only increase pH but also lead to the deposition of calcite (Fig. 13A); (2) CO_2 enrichment and mixing, the lost CO_2 enriching in the shallow part together with mixing between magmatic and meteoric waters result in salinity and temperature decreasing (Fig. 13B); (3) decompression, cooling and mixing, the pressure, salinity and temperature decrease continuously resulting from mixing with meteoric water and/or injecting into fractures following the ore-forming fluids migrating to the shallow part (Fig. 13C).

Sources of ore-forming materials

S and Pb isotopes effectively constrain the sources of these elements[60–62]. The $\delta^{34}S$ values of sulfides and barites obtained at Laurani are 1.57–5.55‰ and 24.01–25.90‰ (Table 3), respectively, which are consistent with a magmatic source of sulfur[63]. In Fig. 11, the $\delta^{34}S$ values of hydrothermal sulfate–sulfide pairs from the Laurani deposit and some other Miocene high-sulfidation deposits in the Central Andes show an extension of the trend through the data for igneous apatite–pyrrhotite pairs from Julcani[61], suggesting that the hydrothermal

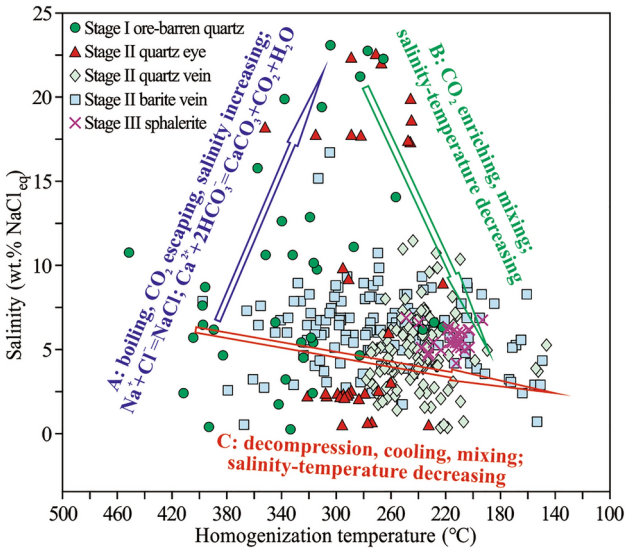

Fig. 13. Evolution processes of ore-forming fluids in the Laurani deposit. Four data with high salinities of 42.1–53.3 wt.% $NaCl_{eq}$ and homogenization temperatures 241 to 261 °C from type IV daughter mineral-bearing inclusions in the stage II quartz eyes are not involved.

fluids are primarily H_2S-dominant fluids[53,61], which is typical for Andean high-sulfidation systems[53,61,64] and is almost always the case for high-sulfidation magmatic–hydrothermal systems[40,61,65]. At Laurani, temperatures of the fractionations between barite and sulfide range from 260 to 300 °C (Fig. 11), coinciding well with the homogenization temperatures of fluid inclusions measured in the related quartz and barite from the stage II. Considering the H_2S-dominant fluids and three limited $\delta^{34}S$ data of barite-sulfide pairs (Fig. 11), we estimate that the bulk $\delta^{34}S$ value ($\delta^{34}S_{\Sigma S}$) for the hydrothermal fluids may be about 2 to 5‰ in the Laurani deposit. This estimate is consistent with the $\delta^{34}S_{\Sigma S}$ observed in hydrothermal fluids from other high-sulfidation epithermal deposits, such as Julcani[61,66] and Pascua[50].

The Pb isotope ratios from various sulfide minerals at Laurani are fairly uniform (Table 4; Fig. 12), indicating that the same Pb source contributes to the Laurani ores. Although no Pb isotope of the Laurani volcanic rocks have been conducted, based on the geological features of deposit[16] and the H, O and S isotope sources discussed above, we infer that these volcanic rocks are the proximal source of lead for mineralization. The Laurani volcanic rocks are generated primarily from the partial melting of the thickened Paleoproterozoic lower crust that related to the Arequipa Massif[19]. The Pb isotope ratios of the Laurani ores (Table 4), are coincident well with the Pb isotopic values of the Arequipa Massif that with $^{206}Pb/^{204}Pb = 16.083–18.551$, $^{207}Pb/^{204}Pb = 15.435–15.650$ and $^{208}Pb/^{204}Pb = 36.712–38.655$[67,68], except for slightly higher $^{208}Pb/^{204}Pb$ ratios. In Fig. 12, the Pb isotope ratios of ores at Laurani lie above those of Nazca plate basalts and Nazca plate metalliferous and pelagic sediments[60], and do not overlap with the Paleozoic and Cretaceous-Tertiary sedimentary rocks[60]. Instead, they lie within or near the Pb isotope ratios of the Arequipa Massif basement, indicating Pb isotopes at Laurani originate primarily from the ancient, high-grade metamorphic basement of the Arequipa Massif. The Pb model ages (T) calculated from the Laurani ores are 231–280 Ma (Table 4), which are older than the Laurani volcanic activity (~ 7.5 Ma) at the time when the Altiplano uplifted rapidly (~ 10–6 Ma), indicating a significant "delay" in radiogenic Pb ingrowth and an ancient basement beneath the Altiplano. Furthermore, the two characteristic geochemical parameters of metal sources μ ($^{238}U/^{204}Pb$) and κ ($^{232}Th/^{238}U$) calculated from the Laurani ores with a mean value of 9.5 and 3.9 (Table 4), respectively, are both slightly lower than the μ values (9.6–9.7) and the κ values (4.0–4.2) of the Altiplano estimated by Albarède et al.[69], which also reflect the Pb isotope source of Laurani ores is from an ancient basement, where the continental crust is particularly thick and U has been preferentially removed during orogenic events[69].

Some late Miocene epithermal deposits in the Central Andes have a similar Pb isotope source signature (Fig. 12). For instance, the San Cristobal ores contain about 75% Pb from the metamorphic basement estimated by Kamenov et al.[60], and the Pb isotope ratios of ores at Berenguela, Negrillos, Carangas and Chinchilhuma also reflect the incorporation of Pb from the Proterozoic metamorphic basement underlying the area[60,70,71]. These late Miocene epithermal deposits, including Laurani, are located in Pb isotope Province IV proposed by Kamenov et al.[60] and Macfarlane and Lechtman[71], which have low $^{206}Pb/^{204}Pb$ and $^{207}Pb/^{204}Pb$ values compared to $^{208}Pb/^{204}Pb$ ratios, representing a predominant Pb source from the Arequipa Massif metamorphic basement beneath the Central Andes[67,68].

Implications for the mineralization and deposit model of Laurani

High-sulfidation epithermal deposits typically form contemporaneously and co-spatially with volcanism and associated intrusions[7,8]. Recently, Liu et al.[19] demonstrated that the volcanic activity occurred at ~ 7.5 Ma at Laurani, indicating that the Laurani high-sulfidation epithermal deposit also form in the late Miocene, which is coincident with the episode of major and rapid uplift of the Altiplano[20,21,24,72–76]. Numerous epithermal deposits with comparable metallogenic ages were formed in and around the Altiplano, such as San Cristobal[60], La Española[15,77], Choquelimpie[78], Santa Rosa[79], Veladero[55], among others, which reflect a crucial high-sulfidation magmatic–hydrothermal metallogenic event related to rapid uplift of the Altiplano in the late Miocene.

As above-discussed, various mineralization and hydrothermal alterations observed at Laurani are similar to those in typical polymetallic veins associated to porphyry–high-sulfidation metallogenic system[3,8,80]. Four styles of orebodies occur in diverse shapes, have a close spatial connection with the volcanic rocks, reflecting an intense influence of structural and lithological controls. Additionally, the porphyry-style mineralization within the dacitic porphyry that we first proposed[16,17] indicates there is a great potential to prospect porphyry deposits in the depth of the Laurani mine.

Fluid inclusions in the stage I ore-barren quartz show the fluids predated predominant metal deposition are low- to moderate-salinity, high-temperature and CO_2-bearing fluids, which may be the evolved fluids from phase separation of high temperature (> 500 ℃) magmatic fluids that exsolved from magma chamber at depth (Fig. 14), where may present possibly a high-salinity fluids and cause potassic alteration in the porphyry environment (Fig. 14). The early evolved low- to moderate-salinity fluids then rise and undergo processes of boiling, cooling and mixing to precipitate metal, generating four styles of mineralization and associated alterations (Fig. 14). The origin of the ore-forming fluids that separated from the evolved magmatic fluids and exchanged later with meteoric water is also well documented by the H–O isotopes (Fig. 10).

S–Pb isotopes also constrain that the source of ore-forming materials is a magmatic origin. Furthermore, the Pb isotopic values of Laurani ores indicate that the lead is primarily and initially derived from the Arequipa Massif basement. Combined with the similar epithermal deposits that formed in the late Miocene from the Central Andes, such as those mentioned above, we conclude that during the rapid uplift of the orogenic belt, the partial melting of the thickened lower crust is not only an essential magma formation mechanism[19], but also is a significant source of metal for forming porphyry–epithermal deposits.

Conclusions

The Laurani deposit is a typical high-sulfidation epithermal deposit that related to the contemporaneous volcanic rocks formed at about 7.5 Ma in the late Miocene, which is coeval with the period of major and rapid

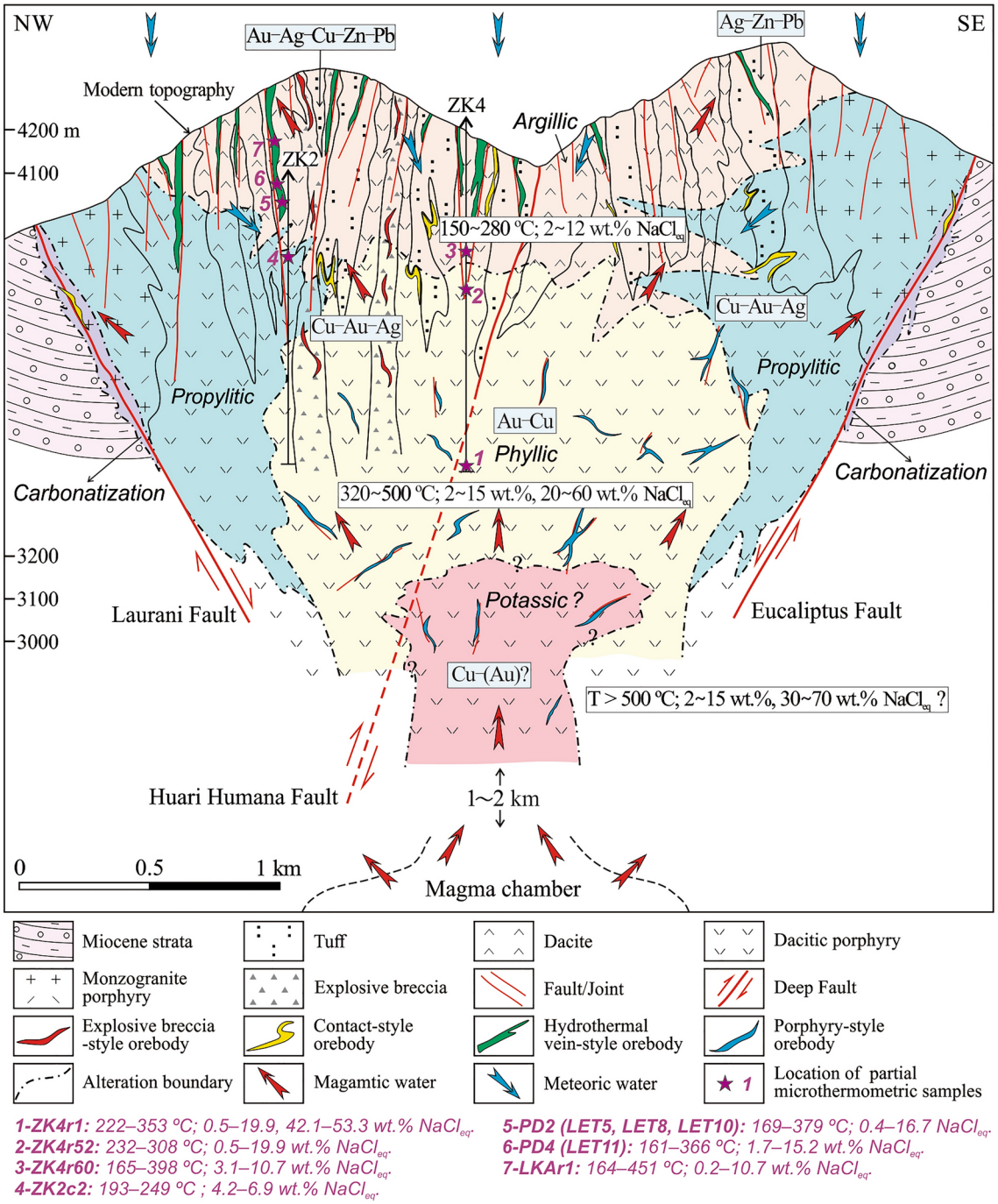

Fig. 14. Metallogenic model of the Laurani deposit.

uplift of the Altiplano plateau. At Laurani, four hydrothermal stages are recognized, with most of the metal precipitated during the stage II and stage III, generating four styles of mineralization with different occurrences that controlled by structures and lithologies. Currently, the hydrothermal vein-style Au–Ag–Cu–Pb–Zn is the most important and economically significant mineralization, developing mainly in the shallow part, while the porphyry-style Au–Cu observed in dacitic porphyry indicates the potential to form porphyry deposits at depth. The intense hydrothermal alterations, particularly the residual vuggy quartz, alunite, barite and alteration zonation of phyllic to propylitic and argillic at Laurani, also reflect it's a typical high-sulfidation epithermal metallogenic systems.

The early ore-forming fluids obtained from the stage I ore-barren quartz demonstrate low- to moderate-salinity and high-temperature (90% of homogenization temperatures > 300 ℃) fluids, then boiling occur about between 250 and 360 ℃, and they transform into low-salinity and low-temperature (90% of homogenization temperatures < 220 ℃) fluids in the late. H–O–S–Pb isotopes are consistent with the predominant magmatic sources of the ore-forming fluids and materials, with a little meteoric water mixing later. S isotopic values of

barite–sulfides from the stage II and stage III, combined with alteration minerals such as vuggy quartz, barite and alunite, suggesting that the ore-forming fluids are acidic, oxidized and H_2S dominant. Pb isotopic values reflect the Pb is initially derived from the Arequipa Massif basement, indicating that the thickened lower crust may be an important metal source for the formation of epithermal deposits.

Data availability

All data generated or analysed during this study are included in this published article and its supplementary tables A, B, C and D.

Received: 23 May 2024; Accepted: 15 November 2024
Published online: 30 December 2024

References

1. Lindgren, W. A suggestion for the terminology of certain mineral deposits. *Econ. Geol.* **17**, 292–294 (1922).
2. Hayba, D.O., Bethke, P.M., Heald, P., Foley, N.K. Geologic, mineralogic and geochemical characteristics of volcanic-hosted epithermal precious metal deposits. In *Geology and Geochemistry of Epithermal Systems* (eds Berger, B. R. et al.) Vol. 2, 129–167 (1985).
3. Hedenquist, J.W., Arribas, A., Gonzales-Urien, E. Exploration for epithermal gold deposits. In *Gold in 2000* (ed. Hagemann, S. G. & Brown, P. E.), Vol. 13, 245–277 (2000).
4. Berger, B. R. & Henley, R. W. Advances in the understanding of epithermal gold-silver deposits, with special reference to the western United States. In *The Geology of Gold Deposits: The Perspective in 1988* (eds Keays, R. R. et al.) Vol. 6, 405–423 (1989).
5. White, N. C. & Hedenquist, J. W. Epithermal environments and styles of mineralization: Variations and their causes, and guidelines for exploration. *J. Geochem. Explor.* **36**, 445–474 (1990).
6. White, N. C. & Hedenquist, J. W. Epithermal gold deposits: Styles, characteristics and exploration. *SEG Newsl.* **23**, 1–13 (1995).
7. Sillitoe, R. H. & Hedenquist, J. W. Linkages between volcanotectonic settings, ore fluid compositions, and epithermal precious metal deposits. In *Volcanic, Geothermal, and Ore-Forming Fluids: Rulers and Witnesses of Processes within the Earth* (eds Simmons, S. F. & Graham, I.) Vol. 10, 315–343 (2005).
8. Simmons, S. F., White, N. C. & John, D. A. Geological characteristics of epithermal precious and base metal deposits. In *Economic Geology 100th Anniversary Volume* (eds Hedenquist, J. W. et al.), 485–522 (2005).
9. Tosdal, R. M., Dilles, J. H. & Cooke, D. R. From source to sinks in auriferous magmatic-hydrothermal porphyry and epithermal deposits. *Elements* **5**, 289–295 (2009).
10. Seedorff, E. et al. Porphyry deposits: characteristics and origin of hypogene features. In *Economic Geology 100th Anniversary Volume* (eds. Hedenquist, J. W. et al.), 251−298 (2005).
11. Cooke, D. R., Deyell, C. L., Waters, P. J., Gonzales, R. I. & Zaw, K. Evidence for magmatic-hydrothermal fluids and ore-forming processes in epithermal and porphyry deposits of the Baguio district, Philippines. *Econ. Geol.* **106**, 1399–1424 (2011).
12. Ahlfeld, F. Metallogenetic Epochs and Provinces of Bolivia. *Mineralium Deposita* **2**, 291–311 (1967).
13. Redwood, S. D. & Macintyre, R. K-Ar dating of Miocene magmatism and related epithermal mineralization of the northeastern Altiplano of Bolivia. *Econ. Geol.* **84**, 618–630 (1989).
14. Cunningham, C. G., Mcnamee, J., Vásquez, J. P. & Ericksen, G. E. A model of volcanic dome-hosted precious metal deposits in Bolivia. *Econ. Geol.* **86**, 415–421 (1991).
15. Arce-Burgoa, O. R. & Goldfarb, R. J. Metallogeny of Bolivia. *SEG Newsl.* **79**, 8–15 (2009).
16. Liu, F. et al. Geological characteristics and ore-controlling factors of Laurani porphyry-epithermal deposit, Bolivia. *Mineral Deposits* **41**, 138–157 (2022) (**in Chinese with English abstract**).
17. Liu, F., Han, R. S., Wang, J. S. & Li, W. Y. Alteration and mineralization types of the Laurani porphyry deposit in Central-Andean metallogenic belt, Bolivia. *Acta Geologica Sinica (English Edition)* **S1**, 220–221 (2017).
18. Redwood, S. D. & Rice, C. M. Petrogenesis of Miocene basic shoshonitic lavas in the Bolivian Andes and implications for hydrothermal gold, silver and tin deposits. *J. S. Am. Earth Sci.* **10**, 203–221 (1997).
19. Liu, F. et al. Geochronology and petrogenesis of volcanic rocks in the Laurani epithermal Au-Ag-Cu deposit, northern Bolivian Altiplano. *J. S. Am. Earth Sci.* **120**, 104044 (2022).
20. Garzione, C. N., Molnar, P., Libarkin, J. C. & MacFadden, B. J. Rapid late Miocene rise of the Bolivian Altiplano: Evidence for removal of mantle lithosphere. *Earth Planet. Sci. Lett.* **241**, 543–556 (2006).
21. Isacks, B. L. Uplift of the central Andean plateau and bending of the Bolivian orocline. *J. Geophys. Res.* **93**, 3211–3231 (1988).
22. Allmendinger, R. W., Jordan, T. E., Kay, S. M. & Isacks, B. L. The evolution of the Altiplano-Puna plateau of the central Andes. *Annu. Rev. Earth Planet. Sci.* **25**, 139–174 (1997).
23. Arriagada, C., Roperch, P., Mpodozis, C. & Cobbold, P. Paleogene building of the Bolivian Orocline: tectonic restoration of the central Andes in 2-D map view. *Tectonics* **27**, 1–14 (2008).
24. Scott, E. M. et al. Andean surface uplift constrained by radiogenic isotopes of arc lavas. *Nat. Commun.* **9**, 1–8 (2018).
25. Lamb, S. & Hoke, L. Origin of the high plateau in the Central Andes, Bolivia, South America. *Tectonics* **16**, 623–649 (1997).
26. Horton, B. K., Hampton, B. A. & Waanders, G. L. Paleogene synorogenic sedimentation in the Altiplano plateau and implications for initial mountain building in the central Andes. *Geol. Soc. Am. Bull.* **113**, 1387–1400 (2001).
27. Horton, B. K. Sedimentary record of Andean mountain building. *Earth-Sci. Rev.* **178**, 279–309 (2018).
28. Keller, P., Paar, W. H. & Dunn, P. J. Lammerit, $Cu_3[AsO_4]_2$, ein neues mineral von Laurani. *Bolivien. Tschermaks mineralogische and petrographische mitteilungen* **28**, 157–164 (1981).
29. Paar, W. H. et al. Braithwaiteite, $NaCu_5(TiSb)O_2(AsO_4)_4[AsO_3](OH)]_2(H_2O)_8$, a new mineral species from Laurani, Bolivia. *Can. Mineral.* **47**, 947–952 (2009).
30. Roedder, E. Fluid inclusions. In *Reviews in mineralogy* (ed. Ribbe, P. H.) Vol. 12, 1–664 (1984).
31. Lu, H.Z., Fan, H.R., Ni, P., Ou, G.X., Shen, K., Zhang, W.H. *Fluid Inclusions* 1–450 (Science Press, 2004). (**in Chinese**)
32. Bodnar, R. J. Reviced equation and table for determining the freezing point depression of H_2O-NaCl solutions. *Geochimica et Cosmochimica Acta* **57**, 683–684 (1993).
33. Hall, D. L., Sterner, S. M. & Bodnar, R. J. Freezing point depression of NaCl-KCl-H_2O solutions. *Econ. Geol.* **83**, 197–202 (1988).
34. Collins, P. L. Gas hydrates in CO_2-bearing fluid inclusions and the use of freezing data for estimation of salinity. *Econ. Geol.* **74**, 1435–1444 (1979).
35. Clayton, R. N. & Mayeda, T. K. The use of bromine pent a fluoride in the extraction of oxygen from oxides and silicates for isotope analysis. *Geochimica et Cosmochimica Acta* **27**, 43–52 (1963).
36. Robinson, B. W. & Kusakabe, M. Quantitative preparation of sulfur dioxide, for $^{34}S/^{32}S$ analyses, from sulfides by combustion with cuprous oxide. *Anal. Chem.* **47**, 1179–1181 (1975).
37. Clayton, R. N., Goldsmith, J. R., Karel, K. J. & Mayeda, T. K. Limits on the effect of pressure on isotopic fractionation. *Geochimica et Cosmochimica Acta* **39**, 1197–1201 (1975).

38. Kusakabe, M. & Robinson, B. W. Oxygen and sulfur isotope equilibria in the $BaSO_4$-HSO_4- H_2O system from 110 to 350°C and applications. *Geochimica et Cosmochimica Acta* **41**, 1033–1040 (1977).
39. Faure, G. *Principles of Isotope Geology, Second Edition* (New York: John Wiley & Sons), 1–589 (1986).
40. Arribas, A. Characteristics of high-sulfidation epithermal deposits and their relation to magmatic fluid. In *Magmas, Fluids, and Ore Deposits* (ed. Thompson, J. F. H.), Vol. 23, 419–454 (1995).
41. Vasyukova, O. V., Kamenetsky, V. S., Goemann, K. & Davidson, P. Diversity of primary CL textures in quartz from porphyry environments: implication for origin of quartz eyes. *Contrib. Mineral. Petrol.* **166**, 1253–1268 (2013).
42. Leng, C. B. et al. Lithogeochemical and mineral chemical footprints of porphyry Cu±Mo±Au deposits: a review. *Acta Geologica Sinica* **94**, 3189–3212 (2020) (**in Chinese with English abstract**).
43. Bodnar, R.J., Lecumberri-Sanchez, P., Moncada, D. & Steele-MacInnis, M. Fluid inclusions in hydrothermal ore deposits. In *Treatise on Geochemistry, Second Edition* (ed. Holland, H. D. & Turekian, K. K.), Vol. 13, 119–142 (2014).
44. Taylor, H. P. The application of oxygen and hydrogen isotope studies to problems of hydrothermal alteration and ore deposit. *Econ. Geol.* **69**, 843–883 (1974).
45. Ni, P. et al. Genesis of the Late Jurassic Shizitou Mo deposit, South China: evidences from fluid inclusion, H-O isotope and Re-Os geochronology. *Ore Geol. Rev.* **81**, 871–883 (2017).
46. Wang, Y. H., Zhang, F. F. & Li, B. C. Genesis of the Yandong porphyry Cu deposit in eastern Tianshan, NW China: Evidence from geology, fluid inclusions and isotope systematics. *Ore Geol. Rev.* **86**, 280–296 (2017).
47. Hajsadeghi, S., Mirmohammadi, M. & Asghari, O. Evidence of gas plume model in porphyry copper deposits based on anatomy, fluid inclusions and H-O isotopes: Insight from Kahang deposit, Iran. *Ore Geol. Rev.* **139**, 104517 (2021).
48. Deen, J. A., Rye, R. O., Munoz, J. L. & Drexler, J. W. The magmatic hydrothermal system at Julcani, Peru: evidence from fluid inclusions and hydrogen and oxygen isotopes. *Econ. Geol.* **89**, 1924–1938 (1994).
49. Beuchat, S., Moritz, R. & Pettke, T. Fluid evolution in the W-Cu–Zn–Pb San Cristobal vein, Peru: fluid inclusion and stable isotope evidence. *Chem. Geol.* **210**, 201–224 (2004).
50. Deyell, C. L. et al. Alunite in the Pascua-Lama high-sulfidation deposit: constraints on alteration and ore deposition using stable isotope geochemistry. *Econ. Geol.* **100**, 131–148 (2005).
51. Fifarek, R. H. & Rye, R. O. Stable-isotope geochemistry of the Pierina high-sulfidation Au–Ag deposit, Peru: influence of hydrodynamics on SO2− 4–H_2S sulfur–isotope exchange in magmatic-steam and steam-heated environments. *Chem. Geol.* **215**, 253–279 (2005).
52. Baumgartner, R., Fontboté, L. & Vennemann, T. Mineral zoning and geochemistry of epithermal polymetallic Zn-Pb-Ag-Cu-Bi mineralization at Cerro de Pasco, Peru. *Econ. Geol.* **103**, 493–537 (2008).
53. Cerpa, L. M. et al. Lithologic controls on mineralization at the Lagunas Norte high-sulfidation epithermal gold deposit, northern Peru. *Miner Deposita* **48**, 653–673 (2013).
54. Catchpole, H., Kouzmanov, K., Putlitz, B., Seo, J. H. & Fontboté, L. Zoned base metal mineralization in a porphyry system: Origin and evolution of mineralizing fluids in the Morococha district, Peru. *Econ. Geol.* **110**, 39–71 (2015).
55. Holley, E. A., Monecke, T., Bissig, T. & Reynolds, T. J. Evolution of high-level magmatic-hydrothermal systems: New insights from ore paragenesis of the Velader high-sulfidation epithermal Au-Ag deposit, El Indio-Pascua belt, Argentina. *Econ. Geol.* **112**, 1747–1771 (2017).
56. Henley, R. W. & Berger, B. R. Magmatic-vapor expansion and the formation of high-sulfidation gold deposits: Chemical controls on alteration and mineralization. *Ore Geol. Rev.* **39**, 63–74 (2011).
57. Redmond, P. B., Einaudi, M. T., Inan, E. E., Landtwing, M. R. & Heinrich, C. A. Copper deposition by fluid cooling in intrusion-centered systems: New insights from the Bingham porphyry ore deposit, Utah. *Geology* **32**, 217–220 (2004).
58. Pudack, C., Halter, W. E., Heinrich, C. A. & Pettke, T. Evolution of magmatic vapor to gold-rich epithermal liquid: The porphyry to epithermal transition at Nevados de Famatina, northwest Argentina. *Econ. Geol.* **104**, 449–477 (2009).
59. Chen, H. & Wu, C. Metallogenesis and major challenges of porphyry copper systems above subduction zones. *Sci. China Earth Sci.* **63**, 899–918 (2020).
60. Kamenov, G., Macfarlane, A. W. & Riciputi, L. Sources of Lead in the San Cristobal, Pulacayo, and Potosí Mining Districts, Bolivia, and a Reevaluation of Regional Ore Lead Isotope Provinces. *Econ. Geol.* **97**, 573–592 (2002).
61. Rye, R. O. A review of the stable-isotope geochemistry of sulfate minerals in selected igneous environments and related hydrothermal systems. *Chem. Geol.* **215**, 5–36 (2005).
62. Harkins, S. A. Lead Isotope analysis of non-sulfide zinc and sulfide zinc-lead deposits in the Flinders Ranges, South Australia. *Econ. Geol.* **103**, 353–364 (2008).
63. Ohmoto, H., Rye, R.O. Isotopes of sulfur and carbon. In *Geochemistry of Hydrothermal Ore Deposits, Second Edition* (ed Barnes, H. L.), 509–567 (1979).
64. Rainbow, A. Genesis and evolution of the Pierina high-sulphidation epithermal Au-Ag Deposit, Ancash, Peru. Ph.D thesis 1–277 (Queen's University, 2009).
65. Rye, R. O. The evolution of magmatic fluids in the epithermal environment: the stable isotope perspective. *Econ. Geol.* **88**, 733–753 (1993).
66. Deen, J.A. Hydrothermal ore deposition related to high-level igneous activity: a stable-isotopic study of the Julcani mining district, Peru. Ph.D thesis 1–246 (University of Colorado, 1990).
67. Mamani, M., Tassara, A. & Wörner, G. Composition and structural control of crustal domains in the central Andes. *Geochem. Geophys. Geosyst.* **9**, 1–13 (2008).
68. Ramos, V. A. The basement of the Central Andes: the Arequipa and related terranes. *Annu. Rev. Earth Planet. Sci.* **36**, 289–324 (2008).
69. Albarède, F., Desaulty, A. M. & Blichert-Toft, J. A geological perspective on the use of Pb isotopes in archaeometry. *Archaeometry* **54**, 853–867 (2012).
70. Tosdal, R. M. et al. Summary of Pb isotopic compositions in epithermal precious metal deposits, Orcopampa area of southern Peru, Berenguela area of western Bolivia, and Maricunga Belt in north-central Chile. In *Investigaciones de metales preciosos en el complejo volcánico Neógeno-Cuaternario de los Andes Centrales* 47–55 (Servicio Geológico de Bolivia, 1993).
71. Macfarlane, A. W. & Lechtman, H. N. Andean ores, bronze artifacts, and lead isotopes: constraints on metal sources in their geological context. *J. Archaeol. Method Theory* **23**, 1–72 (2016).
72. Sempere, T., Hérail, G., Oller, J. & Bonhomme, M. G. Late Oligocene-early Miocene major tectonic crisis and related basins in Bolivia. *Geology* **18**, 946–949 (1990).
73. Ghosh, P., Garzione, C. N. & Eiler, J. M. Rapid uplift of the Altiplano revealed through ^{13}C–^{18}O bonds in paleosol carbonates. *Science* **311**, 511–515 (2006).
74. Garzione, C. N. et al. Rise of the Andes. *Science* **320**, 1304–1307 (2008).
75. Armijo, R., Lacassin, R., Coudurier-Curveur, A. & Carrizo, D. Coupled tectonic evolution of Andean orogeny and global climate. *Earth-Sci. Rev.* **143**, 1–35 (2015).
76. Kar, N., Garzione, C. N., Jaramillo, C. & Shanahan, T. M. Rapid regional surface uplift of the northern Altiplano plateau revealed by multiproxy paleoclimate reconstruction. *Earth Planet. Sci. Lett.* **447**, 33–47 (2016).
77. Arce-Burgoa, O.R. Metalliferous ore deposits of Bolivia, Second Edition, 1–233 (La Paz: SPC Impresores S.A., 2009).
78. Gröpper, H. et al. The epithermal gold-silver deposit of Choquelimpie, northern Chile. *Econ. Geol.* **86**, 1206–1221 (1991).

79. Morche, W., Velasco, C., Loayza, D. & Clark, A. *Late Miocene High-sulfidation Epithermal Gold Deposits of the Aruntani District, Southern Peru. Congreso Geologico del Peru* (Sociedad Geologica del Peru, 2008).
80. Sillitoe, R. H. Porphyry copper systems. *Econ. Geol.* **105**, 3–41 (2010).
81. SERGEOMIN-YPFB (Servicio Nacional de Geologia y Mineria, Yacimientos Petroliferos Fiscales Bolivianos). Map geologico de Bolivia (Escala 1:1000000), (2001).
82. Campbell, A. R., Rye, D. & Petersen, U. A hydrogen and oxygen isotope study of the San Cristobal Mine, Peru; implications of the role of water to rock ratio for the genesis of wolframite deposits. *Econ. Geol.* **79**, 1818–1832 (1984).
83. Savin, S. M. & Epstein, S. The oxygen and hydrogen isotope geochemistry of clays minerals. *Geochim. Cosmochim. Acta* **34**, 24–42 (1970).
84. Campbell, A. R. A sulfur isotopic study of the San Cristobal tungsten-base metal mine. *Peru. Mineralium Deposita* **22**, 42–46 (1987).
85. Rainbow, A., Clark, A. H., Kyser, T. K., Gaboury, F. & Hodgson, C. J. The Pierina epithermal Au–Ag deposit, Ancash, Peru: paragenetic relationships, alunite textures, and stable-isotope geochemistry. *Chem. Geol.* **215**, 235–252 (2005).

Acknowledgements

This work was co-financed by the China National Key Research and Development Program (Grant No. 2018YFC0603902), the Program of 'Yunling Scholar' of Yunnan province (2014), Projects of Yunnan Engineering Laboratory of Mineral Resources Prediction and Evaluation (YM Lab) (2011) and Innovation Team of Yunnan province and KMUST (2008, 2012). We also would like to thank EMPRESA MINERA Thaya Motaña S.A and Yunnan Metallurgical Resources Co., Ltd for their useful helps.

Author contributions

Fei Liu: writing—review and editing, conceptualization. Runsheng Han: project administration, funding acquisition, conceptualization. Shuming Wen: supervision. Wenyao Li: resources. Li Lei: resources. Yuxinyue Guo: data curation.

Declarations

Competing interests

The authors declare no competing interests.

Additional information

Supplementary Information The online version contains supplementary material available at https://doi.org/10.1038/s41598-024-80179-7.

Correspondence and requests for materials should be addressed to R.H. or D.Z.